

1
2
3
4
5
6
7
8
9
10
11
12
13
14
15
16
17
18
19
20
21
22

**A lumped bubble capacitance model controlled by matrix structure to describe
layered biogenic gas bubble storage in shallow subtropical peat**

Xi Chen^{1,2,*}, Xavier Comas³, Andrew Binley⁴, Lee Slater¹

1. Department of Earth & Environmental Sciences, Rutgers University, Newark, NJ

07102, USA

2. State Key Laboratory of Earth Surface Processes and Resource Ecology, Beijing

Normal University, Beijing 100875, China

3. Department of Geosciences, Florida Atlantic University, Davie, FL 33314, USA

4. Lancaster Environment Centre, Lancaster University, Lancaster LA1 4YQ, UK

Correspondence to: X. Chen (chenxioffice@gmail.com)

23 **Abstract**

24 Methane (CH₄) accumulates in the gaseous phase in peat soils, being released to the
25 atmosphere at rates higher than those for diffusion and plant-mediated pathways. An
26 understanding of the mechanisms regulating gas bubble storage in peat remains
27 incomplete. We developed a layered capacitance model to compare the bubble storage
28 ability of peat over different depths. A peat monolith (0.395 m × 0.243 m × 0.247
29 m) was collected from the US Everglades and kept submerged for 102 days from a
30 condition of minimum bubble storage to bubble saturation. Time-lapse
31 electromagnetic wave velocity and power spectrum data were used to estimate
32 changes in both gas content and relative average dimensions of stored bubbles with
33 depth. Bubble capacitance, defined as the increase in volumetric gas content (m³ m⁻³)
34 divided by the corresponding pressure (Pa), ranges from 3.3 × 10⁻⁴ to 6.8 × 10⁻⁴ m³
35 m⁻³ Pa⁻¹, with a maximum at 5.5 cm depth of. Bubbles in this hotspot were larger
36 relative to those in deeper layers, whilst the decomposition degree of the upper layers
37 was generally smaller than that of the lower layers. X-ray computed tomography on
38 peat sections identified a specific depth with a low void ratio, and likely regulating
39 bubble storage. Our results suggest that bubble capacitance is related to (1) the
40 difference in size between bubbles and peat pores, and (2) the void ratio. Our work
41 suggests that changes in bubble size associated with variations in water level driven
42 by climate change will modify bubble storage in peat soils.

43

44

45

46 **Keywords:** Peat, methane storage, gas bubbles, lumped capacitance model, X-ray

47 computed tomography, pore structure

48

49

50

51

52

53

54

55

56

57

58

59

60

61

62

63

64

65

66

67 **1. Introduction**

68 Following almost one decade of stable values in the 1990s, the atmospheric
69 concentration of methane (CH₄), the second most important greenhouse gas, has
70 increased since 2007, mandating a higher Global Warming Potential (GWP) in the
71 most recent IPCC (Intergovernmental Panel on Climate Change) report (IPCC, 2013)
72 relative to the previous assessment (IPCC, 2007). The IPCC notes that peatlands may
73 contribute to the variability and uncertainty of global CH₄ emissions (Ciais et al.,
74 2014). In peat soils, CH₄ is produced by methanogens under anaerobic conditions, and
75 released to the atmosphere via three pathways: diffusion, transport through vascular
76 plants and bubbling of CH₄-enriched gas, i.e. ebullition. The contribution of peat soils
77 to the global CH₄ flux is underestimated when CH₄-enriched gas bubbles are
78 neglected, especially as the upward transport and ebullition of CH₄-enriched gas
79 bubbles is suggested to be the dominant pathway for CH₄ emission in peatlands
80 (Coulthard et al., 2009; Glaser et al., 2004). A detailed description of the storage of
81 gas bubbles needed to supply ebullition is lacking (Ebrahimi & Or, 2017; Granberg et
82 al., 2001), in part due to the scale discrepancy between the apparent CH₄ fluxes
83 measured over a whole peat column and the physical properties of a small peat section
84 that control CH₄-enriched gas bubble storage. A layered model structure to describe
85 field-scale ebullition emissions from a mudflat of an estuarine temperate marsh was
86 recently proposed (Chen et al., 2017). In this paper, we use a general lumped
87 capacitance model (Frank et al., 2006) as a conceptual framework to quantify the
88 differences in bubble storage ability between layers of a peat monolith.

89

90 Two basic assumptions are considered in early computational models of bubble
91 storage, corresponding to two stages: In stage 1, the initial CH₄ transfer from the
92 dissolved to gaseous phase is assumed to start when the sum of the partial pressures of
93 all gases in a gas bubble is larger than the total ambient pressure including
94 atmospheric pressure, hydrostatic pressure and the pressure to move soil particles
95 (Rothfuss & Conrad, 1994; Walter et al., 1996). Assuming biogenic CH₄ is the major
96 volatile component in peats and other wetland soils, a critical partial pressure of CH₄
97 can be estimated for initial bubble formation, e.g. 260 matm at 10 degrees Celsius,
98 equivalent to a dissolved CH₄ concentration of 500 μM (8.0 mg L⁻¹), or a constant
99 mixing ratio of 25% CH₄ in the bubble (Shannon et al., 1996; Walter et al., 1996).
100 These homogenous thresholds were based on consideration of the equilibrium
101 concentrations, i.e. the solubility of CH₄ in water, e.g. Hutchison (1957). In stage 2,
102 given that peat and other wetland soils are very porous, most gas bubbles (~70%
103 amount) are assumed to be released immediately to the atmosphere after formation
104 (Walter et al., 1996; Walter & Heimann, 2000), and remaining gas bubbles are
105 assumed to be trapped until the water table drops below the depth where they are
106 located, or until the percentage of the pore space dominated by gas bubbles exceeds a
107 certain critical threshold (~30%) (Walter et al., 1996).

108

109 However, continuous observations of the gas content of peat samples during
110 controlled incubations (Baird et al., 2004; Beckwith & Baird, 2001) suggest that

111 bubbles can grow at CH₄ concentrations below the equilibrium concentrations
112 referenced above (e.g. 8 mg L⁻¹). Observations in organic-rich sediments, e.g. Martens
113 & Albert (1994) also indicate that degree of supersaturation of CH₄ in near-surface
114 pores is not high enough for direct initial formation of a bubble in a water body, i.e.
115 homogeneous nucleation. A reasonable explanation for bubble accumulation under
116 relatively low pore-water CH₄ concentrations is heterogeneous nucleation that starts
117 with a gas nucleus trapped on a solid particle surface (Boudreau, 2012). Jones et al.
118 (1999) suggest that a key requirement for heterogeneous nucleation of gas bubbles is
119 the presence of gas cavities at solid surfaces. The nucleation energy barrier for
120 forming a bubble in a cavity is much lower than in pore water because less interfacial
121 free energy is needed for the bubble to grow (Boudreau, 2012). The tiny crevices
122 where the free gas-liquid surface needed for continuous bubble formation is
123 maintained, are commonly termed nucleation sites.

124

125 Furthermore, CH₄-enriched gas bubbles play an important role in CH₄ storage,
126 possibly containing more CH₄ than the pool of the dissolved phase (Fechner-Levy &
127 Hemond, 1996). A bubble grows outward into the porewater from the solid surface
128 until it is large enough to rise from the nucleation site, breaking away and leaving the
129 nucleus site essentially in its original configuration (Boudreau, 2012) (Figure 1a-c).
130 After detachment from cavities, gas bubbles may enter the atmosphere via two
131 processes. Firstly, bubbles may directly rise unimpeded through pore throats from
132 depth to the surface, resulting in regular steady ebullition (Coulthard et al., 2009)

133 (Figure 1b - 1c). Alternatively, a released bubble may be re-trapped again by a narrow
134 pore throat, generating a new nucleation site, resulting in additional bubble nucleation
135 sites and subsequent accumulation (Li & Yortsos, 1995b; Yortsos & Parlari, 1989)
136 (Figure 1b - 1c). Coulthard et al. (2009) proposed reduced complexity models to
137 simulate bubble dynamics in peat; their results show that the accumulation of bubbles
138 look somewhat like inverted sandpiles. Results from a laboratory observation on
139 ebullition in peat soils support this hypothesis (Ramirez et al., 2015). In fact, trapped
140 gas bubbles in the matrix may act as a buffering reservoir, regulating changes in
141 surrounding dissolved CH₄ concentrations (Granberg et al., 2001). The trapped gas
142 bubbles can be released by environmental forcing or over-accumulation, termed
143 episodic ebullition (Glaser et al., 2004).

144

145 Bubble dimension is a key parameter controlling bubble storage (DelSontro et al.,
146 2015; Kettridge & Binley, 2008; Ramirez et al., 2016; Terry & Slater, 2017). The
147 estimated effective radii of gas bubbles in natural peat vary widely, from less than $1 \times$
148 10^{-5} m (Kettridge & Binley, 2008) to 5×10^{-2} m (Terry & Slater, 2017). A minimum
149 bubble dimension threshold for significant CH₄-enriched gas bubble storage may exist,
150 as the gaseous CH₄ in small bubbles dissolves back to the ambient water more rapidly
151 (DelSontro et al., 2015).

152

153 In this paper, we develop an electrical-circuit-like model from the general lumped
154 capacitance model to explain the layered storage and charge up of CH₄-enriched gas

155 bubbles (Stage 2 referenced above), after initial heterogeneous nucleation in a peat
156 column (Stage 1 referenced above). This conceptual model is applied to discuss the
157 effects of vertical variations in peat structure on bubble storage in a peat monolith.
158 Time-lapse electromagnetic wave speed and power spectra data acquired with a
159 ground penetrating radar (GPR) instrument are used to estimate changes in both
160 volumetric gas content of each layer and the relative average dimensions of stored gas
161 bubbles between depths. X-ray Computed Tomography (CT) on resin-impregnated
162 peat samples from the same monolith is used to determine void ratio variations with
163 depth. Our findings suggest that bubble capacitance of a specific peat layer is directly
164 related to the ratio of pore throat size to gas bubble size, as well as the void ratio.

165

166 **2. Lumped capacitance model of gas bubble storage (charge up) and release** 167 **(discharge)**

168 A layered model of a peat column for bubble storage and release (Figure 1a-1c) was
169 recently proposed (Chen et al., 2017). We build on this work by defining a
170 one-dimensional model consisting of lumped components similar to an electric circuit
171 or a hydraulic circuit (Kirby, 2010). Entrapment (storage) of gas bubbles in pore
172 throats is represented by the dielectric polarization of a capacitor (Figure 1d). Using
173 this analogy, hydraulic/gravitational energy driving the bubble flux is equivalent to
174 the total potential difference provided by a power source, $\Delta\psi_T$. Increasing the
175 volume of entrapped gas bubbles normalized to the total volume of the layer at a
176 depth D , i.e. the volumetric increase in gas content of the layer $\Delta\theta_g$, corresponds to

177 increasing the total stored electric charge Q . Gas bubbles accumulate in pore throats:
178 the average capillary potential over all the bubble entrapping pore throats at depth D
179 increases analogous to the increase in potential difference between the two terminals
180 of the dielectric medium of the capacitor, $\Delta\psi_C$ (Figure 1d). When a resistor is
181 connected to the capacitor in series, the charging rate is regulated by both the resistor
182 and capacitor. The amount of time it takes the resistor-capacitor (RC) circuit to reach
183 a steady state condition, e.g. when the potential difference across the capacitor $\Delta\psi_C$
184 reaches 63% of the full-charge value $\Delta\psi_T$ (Figure S2, Hamilton, 2007), is referred
185 to as the RC time constant τ_c of the circuit. It takes a time $= 7\tau_c$ to reach 0.1% of
186 its full-charge value $\Delta\psi_T$. This time constant τ_c depends on both the capacitance C
187 of the capacitor and the resistance R of the coupled resistor,

$$188 \quad \tau_c = R \times C \quad (1).$$

189 Similarly, bubble resistance R in our conceptual model serves to regulate the bubble
190 accumulation rate associated with layer dimensions (i.e. thickness for the
191 one-dimensional model), pore structure and fluid properties. Table 1 summarizes the
192 analogy between components of an electrical circuit model, water capacitance model
193 and our bubble capacitance model.

194

195 We divide the peat column into n layers ordered from the ground surface (Layer
196 number $i = 1$) to a certain depth D_i ($i = n$), with the surface water layer defined as
197 Layer 0. The water level is maintained at a distance d_0 above the column surface,
198 followed by the n peat layers of equal thickness, $d_i=d$ (Figure 1). The matrix

199 component of each layer is represented by a capacitor (C_i) and a resistor (R_i) in series
200 and the component that each layer contributes to the total water height is represented
201 by a battery cell (potential energy source). The matrices of the individual layers are
202 organized in parallel to express the capacitance of the whole peat column as the sum
203 of the capacitances of all layers (the total gaseous volume is re-normalized to the total
204 volume of all peat layers), whereas the water heights add in series to provide linear
205 partial potential differences corresponding to capacitor-resistor couples. The positive
206 terminal of the i th resistor-capacitor couple is connected to the positive terminal of the
207 corresponding i th battery cell, and all the negative terminals of the resistor-capacitor
208 couples are connected to the negative terminal of the surface battery cell, which is
209 grounded to a reference zero potential. With this arrangement, the potential difference
210 between the two terminals of each resistor-capacitor couple ($\Delta\psi_{Ti}$), represents the
211 cumulative fluid from the bottom of the i th layer to the surface of the overlying water
212 layer, and is expressed in terms of hydraulic pressure (unit: Pa),

$$213 \quad \Delta\psi_{Ti} = \rho_f g D_i, \quad (2)$$

214 where ρ_f is the mass density of the fluid phase, i.e. water density neglecting gas
215 bubbles (997.05 kg m^{-3} at 25° C), g is the gravitational acceleration (9.81 m s^{-2}), and
216 D_i is the depth from the bottom of the i th layer to the water surface,

$$217 \quad D_i = \sum_{k=0}^i d_k \quad (3),$$

218 where d_k represents the thickness of a single layer.

219

220 Our lumped capacitance model assumes that initial gas bubbles already exist and

221 therefore focuses on Stage 2); the initial formation of CH₄-enriched gas bubbles, i.e.
222 Stage 1, can be explained by the general concept of heterogeneous bubble nucleation
223 from gas cavities for various solutions (Jones et al., 1999). Following initial
224 nucleation, gas bubbles grow larger via solution transfer along concentration gradients,
225 crossing the interface between pore water and the gas bubbles (Li & Yortsos, 1995a).
226 The formation of a new gas bubble at an initial heterogeneous nucleation site,
227 subsequent growth and the later detachment from blocking pore throats is regulated
228 by capillary pressure. The buoyancy effect resulting from gravitation has been
229 considered the major energy source driving bubble transport across pore throats in
230 opposition to the capillary effect (Chen & Slater, 2015; Glaser et al., 2004; Tokida et
231 al., 2005).

232

233 In a bubble-filled cavity where the gaseous phase is in equilibrium with the dissolved
234 phase in solution (no growth/no dissolution), the pressure difference between the two
235 sides of the meniscus of the bubble can be described by the Laplace equation for low
236 wetting angles (Clennell et al., 2000; Jones et al., 1999; Li & Yortsos, 1995a).
237 Laboratory and numerical simulations suggest that bubble clusters can branch out
238 from multiple specific nucleation sites to fill the pore network (Li & Yortsos, 1995b;
239 Yousfi et al., 1990) (Figure 1). Therefore, concepts similar to the standard water
240 retention curve can be used to relate volumetric gas content to capillary potential
241 energy for a single peat layer (Figure 2). We divide the relationship between
242 gas/water content and potential energy into three zones based on pressure ranges

243 (Figure 2): Zone I describes regular water retention associated with trapped air
244 bubbles and will not be discussed further; Zone II describes biogenic CH₄-enriched
245 bubble retention of a single layer; Zone III describes highly variable retention mainly
246 resulting from a capacitor breakdown effect.

247

248 We first consider the bubble dynamics associated with Zone II. When the battery cells
249 are connected to the capacitors, indicating submergence by water (Table 1), a
250 transient direct current (DC), representing transient bubble transport, flows through
251 the circuit to charge the capacitors, such that the potential differences across all
252 capacitors starts increasing from zero. Once the potential difference between the
253 terminals of the *i*th capacitor is equal to the corresponding potential difference of the
254 power supply, $\Delta\psi_{Ti}$ (i.e. hydraulic pressure), the capacitor is fully charged and the
255 transient current (i.e. bubble transport via a corresponding branch of the pore network)
256 stops. Then the capacitor acts as an open circuit, i.e. $R_C = \infty$. Analogous to the
257 definition of capillary capacity describing water storage (Richards, 1931) in Zone I,
258 i.e. regular water retention (Figure 2), the term ‘bubble capacitance’ C_i (unit: m³ m⁻³
259 Pa⁻¹) associated with the potential difference $\Delta\psi_{Ti}$ in Zone II describing biogenic
260 CH₄-enriched bubble accumulation is defined as,

261
$$C_i = \frac{\Delta\theta_{g(i)}}{\Delta\psi_{Ti}}, \quad (4)$$

262 where $\Delta\theta_{g(i)}$ (unit: m³ m⁻³) is the maximum change in volumetric gas content from
263 the initial state $\theta_{g(i\text{ini})}$ to the final gas-saturated state $\theta_{g(\text{sat})}$ (Figure 2). Bubble
264 capacitance represents the total volume of gas bubbles held at pore throats in a layer

265 under a specific hydraulic pressure, accounting for variations in bubble size and other
266 factors. The total volume of the gas bubbles stored in the capacitors can decrease by
267 gas bubble transport associated with episodic ebullition. Episodic ebullition events
268 can be driven by decreases in the static hydraulic pressure on the bubbles (Chen &
269 Slater, 2015; Glaser et al., 2004; Tokida et al., 2005), i.e. lowering the applied
270 potential difference $\Delta\psi_{Ti}$.

271

272 We next consider the bubble dynamics occurring in Zone III. Above a particular
273 electric field strength, the dielectric in a capacitor becomes a conductor. The voltage
274 at which this occurs is called the breakdown voltage. However, the breakdown
275 voltage of a material is not a precise value as there is a probability of the material
276 failing at a given voltage. For gas bubbles in peat, once a critical potential difference
277 $\Delta\psi_T$ similar to the breakdown voltage is applied, the i th peat layer no longer behaves
278 as a capacitor but becomes a conductor. Bubble mobility after leaving nucleation sites
279 is high as gas bubbles are relatively small, traveling freely through the interconnected
280 pore space during stage 2 (Beckwith & Baird, 2001; Chen & Slater, 2015; Rosenberry
281 et al., 2006). This effect may result in highly variable gas retention as observed in
282 hydrate-controlled methane seepage from continental margin sediments (Berndt et al.,
283 2014). Therefore, the shape of the corresponding curve is uncertain and not plotted on
284 Figure 2.

285

286 **3. Observation Methodologies**

287 **3.1. Site and sample collection**

288 Laboratory observations were performed on a submerged peat monolith extracted
289 from Water Conservation Area 3 (WCA-3) in the US Florida Everglades (Figure 3a).
290 The site corresponds to one of the locations included in the study by Wright & Comas
291 (2016), has a thickness of 0.72 m, and is characterized predominantly by Loxahatchee
292 peat, thus dominated by water lily (*Nymphaea odorata*) plant species with a typical
293 organic content of 92% (Craft and Richardson, 2008). The site is located in a slough,
294 and is perennially inundated with an average water depth of 0.5 m.

295

296 A peat monolith was extracted by pushing a plastic mould box, with bottom and top
297 removed, into the ground and then digging out the base with a saw (Comas & Slater,
298 2007; Parsekian et al., 2012). The monolith was cut in the laboratory (0.395 m in
299 length L , 0.243 m in width W , and 0.247 m in height H , Figure 3b), transferred into a
300 fitted sample box and equipped with non-invasive sensors and instruments similar to
301 that described in Chen & Slater (2015).

302

303 **3.2. Noninvasive observations of bubble accumulation and release**

304 Laboratory observations, divided into three stages, were made over 102 days (5 Jun
305 2014 - 14 Sep 2014). Stage I involved bubble accumulation under constant conditions
306 of water level, atmospheric pressure and temperature to charge the ‘bubble capacitors’
307 of the peat monolith (from Day 1 to Day 53). Stage II involved environmental-forcing

308 to generate episodic ebullition events that discharge bubble capacitors (from Day 54
309 to Day 67). During this stage, a flow-through chamber device measured CH₄
310 concentration of the air in the headspace above the peat surface to determine the CH₄
311 concentration of the bubbles released by changing water levels. Stage III involved
312 bubble accumulation under constant conditions of water level again to recharge those
313 lost in Stage II, until reaching a saturated state captured in the GPR data, depending
314 on the capacitance C_i of each layer (from Day 68 to Day 102).

315 **3.2.1. Electromagnetic sensing of bubble concentration and average relative** 316 **dimension**

317 **3.2.1.1. Configuration of GPR instrument and visual validation**

318 A GPR instrument equipped with a high frequency antenna (central frequency = 1200
319 MHz, MALÅ Geoscience, Sweden) was used to record the reflected electromagnetic
320 waves from the interface between side of the container and the side of the peat
321 monolith (Figure 3b). These signals were used to estimate variations in the total
322 volume (Chen & Slater, 2015; Comas et al., 2007) and also to infer corresponding
323 relative variations in average sizes of the bubbles between depths (Terry & Slater,
324 2017).

325

326 Two sets of measurements (details below) were made with a trade-off between
327 temporal and spatial resolution. High spatial resolution measurements were made at
328 28 depths ranging from 5 cm to 19 cm with a vertical interval $d = 0.5$ cm ($i = 1, 2,$
329 $3, \dots, 28$). Twenty four traces were recorded at each depth between 8 cm to 32 cm

330 from the left side of the monolith with a horizontal interval $l = 1$ cm ($j = 1, 2, 3, \dots,$
331 24). The scanned area (0.140 m \times 0.240 m) was smaller than that of the actual
332 monolith side (0.243 m \times 0.395 m) to account for the footprint of the GPR antenna.
333 Four such scans were collected in Stage I (Day 2, Day 18, Day 40 and Day 53) with
334 an additional three scans collected in Stage III (Day 68, Day 89 and Day 102),
335 allowing six time-difference images to be created. Collected signals at all the
336 sampling points (i, j) were used to estimate the changes in volumetric gas contents and
337 then the layered bubble capacitances (Section 3.2.1.2). Four locations P1 ($i=5, j=2$),
338 P2 ($i=5, j=14$), P3 ($i=26, j=2$) and P4 ($i=26, j=14$) were analyzed to compare relative
339 bubble dimension between depths (Terry & Slater, 2017) from the 7 time slices using
340 Matlab [*Mathworks, Inc.* 2012] (Section 3.2.1.3).

341

342 Low spatial resolution measurements at four depths of 5 cm (i.e. layer $i = 1$), 8.5 cm (i
343 = 8), 12 cm ($i = 15$) and 18.5 cm ($i = 28$) with a horizontal interval of 2 cm were made
344 during Stage I only. Two measurements per day (one between 9:00-10:00 and another
345 between 17:00-18:00) were collected from Day 1 to Day 46 to confirm continuous
346 bubble accumulation with a fine temporal sampling interval. Direct observations of
347 bubble accumulation were also made by visual counting of gas bubbles appearing on
348 the transparent edge of the box during Stage I only. Bubble counts as a function of
349 depth were qualitatively estimated by tracing macroscopic bubbles appearing on the
350 side of the tank, with tracings digitized for subsequent analysis (Chen & Slater, 2015;
351 Liu et al., 2016; Ramirez et al., 2015).

352

353 3.2.1.2. Bubble capacitance estimation from changes in gas content

354 To estimate the bubble capacitance C_i (equation 4) of the i th layer, the total volumetric
355 content of accumulated gas bubbles $\Delta\theta_{g(i)}$ was calculated from the difference
356 between the initial volumetric gas content $\theta_{g(i,j,ini)}$ and the final bubble-saturating gas
357 content $\theta_{g(i,j,end)}$,

$$358 \quad \Delta\theta_{g(i)} = \sum_{j=1}^{24} (\theta_{g(i,j,end)} - \theta_{g(i,j,ini)}), \quad (5)$$

359 where the index i indicates different depths of the monolith beginning from the top
360 line of GPR scanning, index j indicates different sub columns referenced to the left
361 edge of the GPR scanning and t indicates date of the observation. We assume
362 minimum gas storage, i.e. the peat column is close to 100% water saturation at the
363 start of the experiment. The bubble capacitances $C_i (i, j)$ [$i = 1, 2, 3, \dots, 28; j = 1, 2,$
364 $3, \dots, 24$] cover a part of the strips of the entire volume (i', j') [$i' = 11, 12, 13, \dots, 38;$
365 $j' = 9, 10, 11, \dots, 32$] due to the footprint of the GPR antenna. Gas content $\theta_{g(i,j,t)}$ is
366 regarded as the difference between total porosity $\phi_{(i,j,t)}$ and water content $\theta_{w(i,j,t)}$,

$$367 \quad \theta_{g(i,j,t)} = \phi_{(i,j,t)} - \theta_{w(i,j,t)} \quad (6).$$

368

369 Bulk dielectric permittivity ε_b of the peat monolith depends on the dielectric
370 permittivity and volume concentration of the three phases (solid, gas and liquid). The
371 bulk relative permittivity ε_b was estimated by correcting the two-way travel time
372 Δt_{em} of the electromagnetic signal through the sample monolith. Assuming low
373 dielectric loss,

374
$$\varepsilon_b = \left(\frac{\nu \Delta t_{em}}{2W} \right)^2, \quad (7)$$

375 where ν is the speed of the electromagnetic wave in free space and W is the distance
 376 between the GPR antenna and reflection interface, i.e. 24.3 cm (Figure 3b). Previous
 377 work directly links the gas content θ_g to the bulk dielectric permittivity ε_b , e.g. with
 378 the Complex Refraction Index Model (CRIM) (Comas et al., 2005, 2011). However,
 379 this requires a reliable estimate of $\phi_{(i,j,t)}$, which proved impractical in this study.
 380 Water content θ_w can instead be estimated from the bulk relative permittivity with
 381 an empirical third order polynomial, e.g. the Topp model for mineral soils (Topp et al.,
 382 1980), avoiding the need for a porosity estimate. A specific polynomial function with
 383 calibrated coefficients for *Sphagnum* peat at high saturation conditions (Kellner &
 384 Lundin, 2001) was directly applied to the sawgrass peat monolith with tolerable
 385 structure bias,

386
$$\theta_w = 3.9 \times 10^{-2} + 3.17 \times 10^{-2} \varepsilon_b - 4.5 \times 10^{-4} \varepsilon_b^2 + 2.6 \times 10^{-6} \varepsilon_b^3 \quad (8).$$

387 Substituting equation (7) into (8), the water contents in different saturation states
 388 $\theta_{w(i,j,t)}$ can be estimated.

389

390 It was not possible to acquire porosity measurements on every individual cell $[i, j]$
 391 within the monolith using a gravimetric method. The differential form of equation (6)
 392 states that the increase in volumetric gas content of each cell approximates the
 393 decrease in volumetric water content,

394
$$\theta_{g(i,j,end)} - \theta_{g(i,j,ini)} = \theta_{w(i,j,ini)} - \theta_{w(i,j,end)} + \Delta\phi_{(i,j)}, \quad (9)$$

395 where $\Delta\phi_{(i,j)}$ is an additional correction term for pore expansion during bubble

396 accumulation (Chen & Slater, 2015). Here, this correction is assumed to be negligible
 397 as the gas contents were lower than the saturation values associated with significant
 398 pore expansion. Therefore, bubble capacitance (C_i) can be calculated from water
 399 content estimates ($\theta_{w(i,j,t)}$) determined from dielectric permittivity measurements with
 400 matrix expansion ignored. Substituting equation (9) into (5), the total increase in
 401 volumetric gas content is,

$$402 \quad \Delta\theta_{g(i)} = \sum_{j=1}^{24} (\theta_{w(i,j,\text{ini})} - \theta_{w(i,j,\text{end})}), \quad (10)$$

403 where the absolute water contents $\theta_{w(i,j,\text{ini})}$ and $\theta_{w(i,j,\text{end})}$ at the start of Stage I and
 404 the end of Stage III, respectively, were determined from GPR measurements.
 405 Substituting equations (2), (3) and (10) into (4), the layer-averaged bubble capacitance
 406 C_i of the i th layer is,

$$407 \quad C_i = \frac{\sum_{j=1}^{24} (\theta_{w(i,j,\text{ini})} - \theta_{w(i,j,\text{end})})}{\rho_f g \sum_{k=0}^i d_k}, \quad (11)$$

408 where the initial water level relative to the peat monolith surface, d_0 , is 5.7 cm.

409

410 The same approach was used to estimate changes in bulk relative permittivity ϵ_b
 411 during the period of higher temporal resolution (twice per day within Stage I). GPR
 412 measurements were acquired at low spatial resolution (four depths with a horizontal
 413 interval of 2 cm). These measurements confirmed the temporal continuity of gas
 414 accumulation due to steady biogenic CH_4 production over a long time period.

415

416 **3.2.1.3. Changes in average bubble dimensions**

417 To obtain some insight into the changes in average bubble dimension during bubble

418 accumulation, the power spectrum of the received GPR signal was calculated
419 following the approach outlined by Cassidy (2008) and Terry & Slater (2017). Comas
420 et al. (2005) suggest that clusters of gas bubbles in peat may result in obvious
421 scattering attenuation in GPR signals. The scattering response is related to signal
422 frequency, or alternatively the corresponding wavelength of the electromagnetic
423 signal relative to average bubble size (Terry & Slater, 2017). Small gas bubbles result
424 in highly frequency-dependent Rayleigh scattering, i.e. less signal attenuation at low
425 frequencies relative to higher frequencies. As gas bubbles grow larger, the scattering
426 response becomes more uniform Mie scattering, whereby different frequencies exhibit
427 similar decay characteristics (Terry & Slater, 2017).

428

429 The total attenuation in the EM signal passing through a multiphase material includes
430 both scattering and absorption components. Forward simulations for reference signals,
431 prior knowledge and appropriate assumptions are necessary to solve the inverse
432 scattering problem, e.g. estimating change in the average dimension of gas bubbles
433 (Terry & Slater, 2017), or the distribution pattern of light nonaqueous-phase liquids
434 (LNAPLs) (Cassidy, 2008). Simulation results using the finite-difference time-domain
435 (FDTD) method show that, in the Rayleigh scattering range, peak frequency shifts
436 toward lower frequencies with increases in the volumetric content of the scattering
437 objects when they meet specific geometrical and spatial distribution conditions
438 (Cassidy, 2008). Terry & Slater (2017) argued that relative changes in the frequency
439 power spectra are mostly sensitive to the changes in size of bubbles accumulating in

440 peat, i.e. bubble size dominates the frequency spectra for peat soils. As gas content
441 increases with increasing bubble size, small frequency shifts in the low-frequency
442 Rayleigh scattering region indicate the dominance of Mie scattering due to the
443 accumulation of relatively large bubbles, as assumed to occur here.

444

445 **3.2.2. Flow-through chamber method for CH₄-enriched bubble release**

446 Controlled pore pressure changes were achieved by slow inflow of water to increase
447 the pressure head above the initial saturated condition, and slow outflow to decrease
448 the pressure head until the initial saturated condition was again achieved (Figure 3b).
449 Raising and lowering the water table of the bottom chamber was performed at a
450 controlled slow rate once daily (Figure 3b).

451

452 The CH₄ flux in the upper chamber above the sample monolith was monitored using a
453 methane analyzer (MA) sealed in a matched calibration shroud (LI-7700, LI-COR
454 Inc.). At the 1 Hz sampling rate of the methane analyzer ($f_{MA}=1$ Hz), a pump
455 transported $2.8\pm 0.1\times 10^{-4}$ m³ of CH₄ containing carrier gas between each time slice (1
456 s). The absolute pore-pressures were measured with three vented pressure transducers
457 (26PC Series, Honeywell Sensing and Control) installed 4.5 cm, 11.5 cm and 18.5 cm
458 below the water table (Figure 3b).

459

460 **3.3. Peat humification and X-ray CT scanning**

461 At the end of the experiment, the peat sample was destructively extracted

462 layer-by-layer to determine the vertical variations in structure from humification
463 estimates and X-ray CT scanning measurements. Degree of humification was
464 estimated for five layers between 0 cm and 24.7 cm depth. Samples from each layer
465 were squeezed by hand to determine the texture and color of peat, and the color of
466 drained water. The von Post standard (von Post, 1922) was used to quantify relative
467 decomposition.

468

469 *Blais* [2005] and *Kettridge and Binley* [2008] demonstrated that it is possible to
470 extract information on pore size and pore continuity from X-ray images. In this
471 research, X-ray computed tomography (CT) scanning was used to measure the
472 corresponding vertical distribution of void ratio hypothesized to control bubble
473 storage. A peat column (height = 24.7 cm, diameter = 4.4 cm) was extracted from the
474 peat monolith with a PVC cylinder with minimum compression, and cut into 18 slices
475 each of height 1.4 cm. To retain the peat structure, each slice was cast by dehydration
476 with acetone and impregnated with low viscosity resin (Alumilite, Kalamazoo, MI;
477 Figure 3c) (Quinton et al., 2008). All peat samples were scanned around the center of
478 rotation with an X-tek Benchtop CT160Xi CT scanner (X-Tek Systems Ltd, UK) and
479 a dual field image intensifier coupled to a digital charged couple device (CCD))
480 (*Kettridge & Binley*, 2008, 2011) at 5 micron resolution. The 360×360 pixels
481 forming the middle region of the central 50 radiographs of each peat section were
482 stacked and used for statistical analysis.

483

484 The histograms of voxel intensities recorded on the peat samples are assumed to
485 represent the combination of two normal distributions (Rezanezhad et al., 2009),
486 corresponding to the peat matrix particles and resin, i.e., pores, respectively. The
487 voxel intensities of all slices of each section were fit with the
488 Expectation-Maximization algorithm for mixtures of univariate normals using
489 RStudio (Version 1.0.136, RStudio, Inc. Boston, MA). To account for variations in
490 CT signal decay between different sections, the voxel number ratios r_1 and r_2
491 representing the number of voxels in the resin intensity range and the number of
492 voxels within the peat particle intensity range to the total number of all voxels
493 respectively, were calculated ($r_1 + r_2 = 1$). The r_1 values indicate relative variations in
494 void ratio between depths, which can be compared with the vertical distribution of
495 bubble capacitances C_i .

496

497 **4. Results**

498 Time-lapse dielectric permittivity measurements provided a 2D image of the
499 accumulation of gas bubbles within the monolith, allowing the computation of bubble
500 capacitances representing the maximum bubble storage ability at different depths. The
501 power spectra of the GPR data provide information on changes in relative bubble
502 dimensions between layers. The flow-through chamber system confirmed that these
503 gas bubbles were CH_4 -enriched, whereas destructive analysis including von Post
504 numbers and X-ray CT measurements identified distinct variations in physical
505 properties of peat with depth in the peat block related to the variations in bubble

506 storage. Specific results relating to each measurement are provided below.

507 **4.1. Changes in gas content and bubble capacitance**

508 Based on the bulk relative permittivity results at high spatial resolution (Figure 4a -
509 4g), the water contents at all 28 measurement depths generally decreased across
510 Stages I and III (Figure 4h - 4k, and 4l - 4n). The time-difference images suggest that
511 gas contents at all 28 measurement depths increased across Stages I and III as a result
512 of bubble accumulation (Figure 4o - 4q, and Figure 4r - 4t), and decreased by bubble
513 release, i.e. ebullition driven by environmental forcing, during Stage II (Figure 4q -
514 4r). These increases in gas content were greatest at 5-10 cm depth (Figure 5a),
515 gradually reaching the maximum gas contents at the end of Stage III (Figure 5b).
516 However, at some locations in this hotspot layer, e.g. point P1 ($i=5, j=2$), the
517 maximum change in gas content $\Delta\theta_{g(5,2)}$ was only 0.57% (Figure 4o - 4t), suggesting
518 that this region remained water-saturated with little gas bubble accumulation over
519 time. The final bubble capacitances C_i (equation (11)) of all layers ranged from $3.3 \times$
520 $10^{-4} \text{ m}^3 \text{ m}^{-3} \text{ Pa}^{-1}$ to $6.8 \times 10^{-4} \text{ m}^3 \text{ m}^{-3} \text{ Pa}^{-1}$, with the maximum value located at 5.5 cm
521 depth (Figure 5c).

522

523 Based on the bulk relative permittivity results at high temporal resolution (Figure 6.a),
524 gas bubbles continuously accumulated at four depths; occasional increases in the bulk
525 relative permittivity highlight decreases in gas content resulting from minor ebullition
526 events. Hand-drawing of gas bubbles observed on the chamber side provided a direct
527 estimation of bubble accumulation (Figure 6b). The areal percentage of macroscopic

528 bubbles in every layer i increased over the initial state. Consistent with the dielectric
529 permittivity results, the largest areal percentage of macroscopic bubbles during the
530 entire measurement period was observed in the 5-10 cm depth layer.

531

532 **4.2. Changes in relative average bubble dimension**

533 Four locations P1 ($i=5, j=2$), P2 ($i=5, j=14$), P3 ($i=26, j=2$) and P4 ($i=26, j=14$) were
534 selected (Figure 4t) for GPR power spectrum analysis to estimate relative changes in
535 bubble dimension between layers during bubble accumulation (P2 and P3 in Figure 7,
536 P1 and P4 in Figure S1 in Supplementary Information). Gas contents at point P2
537 showed the largest increases among these four points (Figure 4o - 4t); the
538 high-frequency peaks in the spectra (Figure 7a) are consistent with the dominance of
539 Mie scattering attenuation (Terry & Slater, 2017), suggesting accumulation of large
540 gas bubbles. Points P1 and P4 are characterized by little continuous change in the
541 spectra (Figure S1a and S1b in Supplementary Information), associated with small
542 changes in gas contents during Stages I and III (Figure 4o - 4t). The small frequency
543 shift at P1 between Day 18 and Day 40 (Figure S1a) is consistent with steady
544 ebullition events, along with a few large bubbles being released into the atmosphere
545 such that the corresponding pore space was invaded by small gas bubbles from deeper
546 layers. Point P3 showed continuous decreases in the amplitudes of the spectra over
547 time (Figure 7b). According to the simulated attenuation patterns (Terry & Slater,
548 2017), the relatively greater attenuation at the high frequencies over time indicates the
549 dominance of Rayleigh scattering attenuation, which can be ascribed to the increases

550 in the number and/or size of gas bubbles. Attenuation due to absorption should be
551 reduced in the presence of gas bubbles because of the high resistivity of the bubbles
552 (Terry & Slater, 2017).

553

554 **4.3. Ebullition during forced changes in hydrostatic pressure**

555 Changes in the CH₄ concentrations recorded during the periods of forced hydrostatic
556 pressure changes are summarized in Table 2. Decreases in average pressure heads
557 ranged from 2.0 cm to 10.4 cm, with an average value of 4.08 cm. Corresponding
558 increases in the CH₄ concentration in the upper chamber Δc ranged from 88.4 mmol
559 m⁻³ to 505.0 mmol m⁻³, with an average value of 252.76 mmol m⁻³, proving that the
560 released gas bubbles are CH₄-enriched relative to the atmospheric concentration.

561

562 **4.4. Peat humification and X-ray CT scanning**

563 The von Post scores for humification degree at five depth intervals (Table 3) indicate
564 that the upper peat (depth 0 - 10 cm) was less decomposed than the lower peat (depth
565 10 - 25 cm). The shallow peat of the upper layer (depth 5 - 10 cm) showed variations
566 in humification degree between H2 to H3, containing a peat fabric, e.g. consisting of
567 undecomposed coarse roots of vascular plants, that retained its overall shape after
568 oven drying (Figure 8a). The lower peat below a depth of 10 cm exhibited a gradual
569 increase in decomposition degree per the von Post score H3 to H5 toward the bottom
570 (Figure 8a). The void ratios r_1 , i.e. the number of voxels in the resin intensity range
571 relative to the total number of all voxels of the CT scanning images (Figure 8a)

572 exhibit two minima (0.06 and 0.18 at depths of 4.9 cm and 18.9 cm, respectively),
573 indicating low void ratios relative to other depths in the monolith. The smallest r_1
574 value at 4.9 cm depth is located just above a peak value of bubble capacitance C at 5.5
575 cm depth (Figure 5c), suggesting a barrier structure limiting vertical movement of
576 bubbles. This suggests that the peat fabric between 5 – 10 cm depth partly regulates
577 gas accumulation (Chen & Slater, 2015; Comas et al., 2011; Glaser et al., 2004;
578 Rosenberry et al., 2003). The r_1 values below 16.1 cm depth are overall smaller than
579 the values for the upper layers between 9.1 cm and 14.7 cm depth, indicating a
580 decrease in void ratio.

581

582 **5. Discussion**

583 The general capacitance model provides a convenient way to physically link peat
584 physical properties to bubble storage and release, leading to new understanding of the
585 controls on bubble storage. We conducted laboratory observations on a subtropical
586 peat monolith for estimating bubble capacitances at different depths and discussing
587 the roles of peat structure. Gas dynamics were inferred from time-lapse changes in
588 volumetric gas content and relative average bubble size estimated from
589 electromagnetic wave velocity and power spectra acquired with the GPR instrument,
590 coupled to CH_4 concentrations of released gas bubbles from the peat sample acquired
591 using a flow-through chamber system. Destructive analysis based on humification
592 estimates combined with X-ray CT scanning identified distinct variations in the
593 physical properties of peat between different depths that seem to dictate changes in

594 gas content and average bubble dimensions. The vertical distribution of computed
595 bubble capacitances C that represent the maximum bubble storage capability of the
596 peat revealed a hotspot layer of bubble storage at 5.5 cm depth, below a barrier zone
597 limiting vertical movement of bubbles.

598 **5.1. Initial source of heterogeneous nucleation sites for bubble formation**

599 Our physical model mainly focuses on bubble accumulation (Stage 2) after initial
600 bubble nucleation (Stage 1). Three possibilities are suggested for the initiation of
601 heterogeneous nucleation sites: Firstly, we assume that micro bubbles form readily
602 and act as seeds for later growth (Baird et al., 2004; Coulthard et al., 2009). These
603 pre-existing seeds can be ascribed to pockets of air bubbles trapped in shallow peat
604 during water-table rise (Baird et al., 2004; Beckwith & Baird, 2001; Coulthard et al.,
605 2009), that grow bigger via inward diffusion of biogenic CH_4 . Secondly, a nucleus
606 may form in a small pore pocket under conditions of super-saturation, although the
607 measured dissolved CH_4 concentration will only represent an ‘average’ value for a
608 much larger volume with mostly low CH_4 concentration. Furthermore, the CH_4
609 concentration in gas bubbles can vary substantially, e.g. between 9% and 77% over
610 time (Mustasaar & Comas, 2017), suggesting significant heterogeneity in dissolved
611 CH_4 concentration in pore water and frequent mass exchange between the gaseous
612 phase and dissolved phase. Spatiotemporal variations in both dissolved and gaseous
613 CH_4 concentration observed by (Mustasaar & Comas, 2017) were ascribed to changes
614 in CH_4 production within the peat sample, probably in relation to changes in plant
615 composition and/or quality of organic matter content making up the hotspot area.

616 Thirdly, Boudreau (2012) suggested that, as much sedimentary material is formed
617 sub-aerially in terrestrial environments, trapping of gas during its formation is likely
618 common. Such gas bubbles retained in the sediments below the peat may enter the
619 overlying peat and become trapped again, acting as heterogeneous nucleation sites.

620

621 **5.2. Effects of peat void ratio on bubble capacitance**

622 Volumetric gas content estimates from dielectric permittivity measurements indicate a
623 hotspot of gas bubble accumulation in the upper layer (e.g. 5.5 cm depth with the peak
624 value of bubble capacitance C), as bubbles are not necessarily released immediately
625 upon formation (Beckwith & Baird, 2001; Rosenberry et al., 2003). Kettridge &
626 Binley (2008) used X-ray Computed Tomography (CT) to describe the distribution of
627 individual gas bubbles within *Sphagnum* peat and corresponding peat structures in the
628 laboratory, and found that most gas bubbles (ranging from 0.1 mm³ to 99.9 mm³)
629 clustered near the surface of a peat sample extracted from ground surface to a depth of
630 13 cm, being consistent with our GPR-based observations on Loxahatchee peat (Point
631 2 in Figure 4t).

632

633 Variations in peat stratigraphy have previously been suggested to regulate bubble
634 storage in specific layers within different soil columns, and control the re-distribution
635 of gas bubbles (Chen & Slater, 2015; Kettridge & Binley, 2008; Wright & Comas,
636 2016). The smallest void ratio r_1 at 4.9 cm depth suggests the presence of a barrier
637 structure in the surface layer, being ascribed to the decay of poorly decomposed roots

638 and stems of vascular plants (Figure 8). This barrier structure is located above the
639 peak value of bubble capacitance C found at 5.5 cm depth (Figure 5c). Variations in
640 the von Post humification metric (Figure 8a) suggest a predominantly two-layer
641 model: the upper layer (e.g. depth 0 - 10 cm) is less decomposed (Quinton et al.,
642 2008). Poorly decomposed materials can form a barrier structure supporting bubble
643 storage immediately below. The lower layer of small r_1 values is associated with more
644 decomposed peat, causing a decrease in the size of particles and interparticle pores
645 with depth, and an increase in the amount of solid material per unit volume (Quinton
646 et al., 2000).

647

648 **5.3. Effects of average bubble dimension on bubble capacitance**

649 Based on the changes in the spectra of the EM waves transmitted through peat (Terry
650 & Slater, 2017), the relative average bubble radii (Figure 7 and Figure S1 in
651 Supplementary material) at different depths can be estimated and compared with the
652 vertical distribution of bubble capacitances C . Although the absorption attenuation of
653 simulated EM signals due to electrical conductivity is larger than that due to scattering
654 across all frequencies investigated, the shape of the power spectra reflects both
655 absorption and scattering contributions, and is particularly sensitive to changes in the
656 size of bubbles accumulating in peat, i.e. bubble size dominates the frequency spectra
657 for peat soils (Terry & Slater, 2017).

658

659 This comparison suggests that more large bubbles accumulate in the upper layer (e.g.

660 Point P2 in Figure 7a) relative to the bottom layer (Point P3 in Figure 7b).
661 Hydroacoustic observations of gas bubbles released from organic-rich lake sediments
662 into the upper water column indicate that ebullition events are mostly composed of
663 large bubbles, e.g. diameter > 14 mm in Kiel harbor, Germany (Greinert & Nützel,
664 2004) or diameter > 10 mm in Lake Wohlen, Switzerland (DelSontro et al., 2015). We
665 assume that large gas bubbles are stored in the upper layer, resulting in the high value
666 of bubble capacitance C at the depth of 5.5 cm (Figure 5), with release of these
667 bubbles into the water body above (Layer 0 in Figure 1).

668

669 A larger volume of a single bubble in the upper layer is consistent with gas bubble
670 expansion due to lower pore pressures in the underlying layers; Differences in the
671 pore-size distribution of the peat sample will lead to differences in the ability of the
672 peat to trap and subsequently release bubbles (Baird et al., 2004). Three-dimensional
673 (3-D) analysis of peat pore structure from previous X-ray CT scanning on peat soils
674 also suggests that the pore network is dominated by a single large pore-size
675 (Rezanezhad et al., 2009). Therefore, only correspondingly larger gas bubbles can be
676 held by these pore throats in the upper layer, as bubbles otherwise directly pass by.
677 Finally, larger bubbles may rise faster than smaller bubbles (Corapcioglu et al., 2004),
678 and thus are more likely to bypass consumption by methanotrophs (Ramirez et al.,
679 2016).

680

681 **5.4. Limitations and extension**

682 The 1D layered model structure represents a significant simplification. Indeed, spatial
683 heterogeneity in bubble storage exists in the horizontal plane as confirmed by the
684 GPR data (e.g. Points 1 and 2 in Figure 4t). Direct visual observation via the clear
685 chamber wall qualitatively supports the vertical variation in gas contents over
686 different depths, but the absolute accuracy is limited because of the wall effect on
687 bubble storage (Chen & Slater, 2015; Liu et al., 2016). The bubble capacitance
688 defined in this paper is focused on the volumetric content of stored gas bubbles.
689 However, CH₄ concentration in gas bubbles was recently found to vary substantially
690 (Mustasaar & Comas, 2017).

691

692 The form of water deserves consideration when applying equation (8) to estimate the
693 volumetric water content for the change in gas content from the bulk relative
694 permittivity of each peat layer. The gas content estimates from equation (8) may be
695 affected by bound water on peat particle surfaces, depending in part on the
696 decomposition degree of the layer (Kellner & Lundin, 2001; Yu et al., 1999). In
697 practice, estimates of bound water needed to improve calibration functions are
698 difficult to obtain, and may not significantly improve the estimation of volumetric
699 water content in pores (Kellner & Lundin, 2001). Structural water that constitutes part
700 of the organic matter lattice has little effect on bulk dielectric properties, compared
701 with that of pore-filling water (Marfunin, 2012).

702

703 Furthermore, the rigidity of the peat skeleton regulates deformation of the pore space.
704 Gas bubbles can enlarge the pore space when the exerted pressure is high enough
705 (Chen & Slater, 2015). Changes in porosity were considered in this paper but were not
706 estimated for each small cell making up the 2D plane due to lack of measurements
707 with sufficient accuracy. In addition, the preparation of the peat samples for CT
708 scanning, involving slicing the peat to remove moisture with acetone followed by
709 impregnating the peat with resin (Quinton et al., 2008), may have caused some
710 shrinkage of the pore network. Alternatively, the peat may secrete wax, making it
711 difficult to image the pore structure (Quinton et al., 2009) and accurately estimate
712 void ratios. Finally, gas bubbles in peat can not only accumulate behind existing
713 bubbles lodged in pore necks [*Baird and Waldron, 2003; Strack et al., 2005; Kellner*
714 *et al., 2006*], as considered in this paper, but also underneath woody layers, or below
715 well-decomposed layers of peat (Glaser et al., 2004; Rosenberry et al., 2003). Under
716 the latter condition, fracture mechanisms similar to those occurring in fine-grained
717 sediments are possible (Jain & Juanes, 2009).

718

719 Our conceptual model is general and applicable to most two-phase fluid problems in a
720 porous matrix, e.g. other soil types and gas components, extending the system state
721 analysis with a lumped element model. The concept of ‘bubble capacitance’ links the
722 gas content to environmental pressures with special water retention curves (Figure 2),
723 suggesting additional controls on bubble storage and release beyond the ideal gas law.
724 Using this concept can improve interpretation of observations of gas bubble formation,

725 accumulation and interaction with matrix structure. Changes in gas content might be
726 estimated from the model if discharging and charging of a bubble capacitor are
727 assumed reversible. However, the hysteresis phenomenon commonly observed in soil
728 moisture retention would have to be considered. The time constant τ_c of the model
729 only represents the maximum time required to release a specific volume of gas
730 bubbles associated with decreases in water level, i.e. the occurrence of individual
731 episodic ebullitions event cannot be accurately predicted with the model.

732

733 **6. Conclusions**

734 Bubble capacitance developed from a general capacitance model provides new
735 understanding of the effects of capillary pressure and peat structure on bubble storage
736 using concepts from electromagnetism and hydrostatics. To explore this model,
737 bubble accumulation in a peat block from a subtropical wetland was observed over
738 102 days. The results highlight a hotspot layer of bubble accumulation at depths
739 between 5 and 10 cm below the monolith surface. Based on the corresponding power
740 spectra of returned electromagnetic energy, bubbles in this shallow hotspot layer were
741 larger relative to those in deeper layers, whilst the degree of decomposition of the
742 upper layers was generally smaller than that of the lower layers based on von Post
743 humification tests. X-ray CT from different depths revealed a barrier structure of low
744 void ratio (r_1) just above this hotspot. Our findings suggest that bubble capacitance of
745 a peat layer is related to (1) the difference in size between gas bubbles and peat pores,
746 and (2) the void ratio, both being a function of peat structure. This work has

747 implications for better understanding how changes in water table elevation associated
748 with climate change and sea level rise (particularly for freshwater wetlands near
749 coastal areas like the US Everglades) may potentially alter bubble sizes, and thus
750 bubble storage in peat soils.

751

752 **Acknowledgements**

753 This material is partly based upon work supported by the National Science
754 Foundation under grant EAR 1623895 and National Oceanic and Atmospheric
755 Administration (NOAA) under grant GC11-337. We thank William Wright (Florida
756 Atlantic University), and Greg Mount (currently at Indiana University of
757 Pennsylvania) for assistance in collecting the peat sample. We thank Vassil
758 Karloukovski (Lancaster University) for providing X-ray CT images and Neil Terry
759 (United States Geological Survey) for valuable discussions regarding scattering
760 phenomena. The first author acknowledges the support of the China Scholarship
761 Council (CSC). Any additional data can be obtained from HydroShare
762 (<http://www.hydroshare.org/resource/762bbda0582744158d845afe0f6f27e0>).

763

764

765

766

767

768

769 **References**

- 770 Baird, A. J., Beckwith, C. W., Waldron, S., & Waddington, J. M. (2004). Ebullition of
771 methane-containing gas bubbles from near-surface Sphagnum peat.
772 *GeophysicalResearchLetters*, *31*(21). <https://doi.org/10.1029/2004GL021157>
- 773 Beckwith, C. W., & Baird, A. J. (2001). Effect of biogenic gas bubbles on water flow
774 through poorly decomposed blanket peat. *WaterResourcesResearch*, *37*(3),
775 551–558. <https://doi.org/10.1029/2000WR900303>
- 776 Berndt, C., Feseker, T., Treude, T., Krastel, S., Liebetrau, V., Niemann, H., ... others.
777 (2014). Temporal constraints on hydrate-controlled methane seepage off Svalbard.
778 *Science*, *343*(6168), 284–287. <https://doi.org/10.1126/science.1246298>
- 779 Boudreau, B. P. (2012). The physics of bubbles in surficial, soft, cohesive sediments.
780 *Marine Petroleum Geology*, *38*(1), 1–18.
781 <https://doi.org/10.1016/j.marpetgeo.2012.07.002>
- 782 Cassidy, N. J. (2008). GPR attenuation and scattering in a mature hydrocarbon spill:
783 A modeling study. *VadoseZoneJournal*, *7*(1), 140–159.
784 <https://doi.org/10.2136/vzj2006.0142>
- 785 Chen, X., & Slater, L. (2015). Gas bubble transport and emissions for shallow peat
786 from a northern peatland: The role of pressure changes and peat structure.
787 *WaterResourcesResearch*, *51*(1), 151–168.
788 <https://doi.org/10.1002/2014WR016268>
- 789 Chen, X., VR Schäfer, K., & Slater, L. (2017). Methane emission through ebullition
790 from an estuarine mudflat: 2. Field observations and modeling of occurrence

791 probability. *WaterResourcesResearch*. <https://doi.org/10.1002/2016WR019720>

792 Ciais, P., Sabine, C., Bala, G., Bopp, L., Brovkin, V., Canadell, J., ... others. (2014).
793 Carbon and other biogeochemical cycles. In *Climate change 2013: the physical*
794 *science basis. Contribution of Working Group I to the Fifth Assessment Report of*
795 *the Intergovernmental Panel on Climate Change* (pp. 465–570). Cambridge
796 University Press.

797 Clennell, M., Henry, P., Hovland, M., Booth, J. S., Winters, W. J., & Thomas, M.
798 (2000). Formation of natural gas hydrates in marine sediments: Gas hydrate
799 growth and stability conditioned by host sediment properties. *Annals New York*
800 *AcademySciences*, 912(1), 887–896.
801 <https://doi.org/10.1111/j.1749-6632.2000.tb06842.x>

802 Comas, X., Slater, L., & Reeve, A. (2005). Spatial variability in biogenic gas
803 accumulations in peat soils is revealed by ground penetrating radar (GPR).
804 *GeophysicalResearchLetters*, 32(8). <https://doi.org/10.1029/2004GL022297>

805 Comas, X., Slater, L., & Reeve, A. (2007). In situ monitoring of free-phase gas
806 accumulation and release in peatlands using ground penetrating radar (GPR).
807 *GeophysicalresearchLetters*, 34(6). <https://doi.org/10.1029/2006GL029014>

808 Comas, X., Slater, L., & Reeve, A. (2011). Atmospheric pressure drives changes in
809 the vertical distribution of biogenic free-phase gas in a northern peatland. *Journal*
810 *Geophysical Research: Biogeosciences*, 116(G4).
811 <https://doi.org/10.1029/2011JG001701>

812 Comas, X., & Slater, L. (2007). Evolution of biogenic gases in peat blocks inferred

813 from noninvasive dielectric permittivity measurements. *WaterresourcesResearch*,
814 43(5). <https://doi.org/10.1029/2006WR005562>

815 Corapcioglu, M. Y., Cihan, A., & Drazenovic, M. (2004). Rise velocity of an air
816 bubble in porous media: Theoretical studies. *WaterresourcesResearch*, 40(4).

817 Coulthard, T., Baird, A., Ramirez, J., & Waddington, J. (2009). Methane dynamics in
818 peat: Importance of shallow peats and a novel reduced-complexity approach for
819 modeling ebullition. *CarbonCycling Northern Peatlands*, 173–185.
820 <https://doi.org/10.1029/2008GM000811>

821 DelSontro, T., McGinnis, D. F., Wehrli, B., & Ostrovsky, I. (2015). Size does matter:
822 Importance of large bubbles and small-scale hot spots for methane transport.
823 *Environmentalscience&technology*, 49(3), 1268–1276.
824 <https://doi.org/10.1021/es5054286>

825 Ebrahimi, A., & Or, D. (2017). Mechanistic modeling of microbial interactions at
826 pore to profile scales resolve methane emission dynamics from permafrost soil.
827 *Journal Geophysical Research: Biogeosciences*.
828 <https://doi.org/10.1002/2016JG003674>

829 Fechner-Levy, E. J., & Hemond, H. F. (1996). Trapped methane volume and potential
830 effects on methane ebullition in a northern peatland. *Limnology Oceanography*,
831 41(7), 1375–1383. <https://doi.org/10.4319/lo.1996.41.7.1375>

832 Frank, P. I., David, P. D., Theodore, L. B., & Lavine, A. S. (2006). *Fundamentals of*
833 *heat and mass transfer (6th ed.)*. JohnWiley and Sons, New York. John Wiley &
834 Sons, Inc, Hoboken, NJ, USA.

835 Glaser, P. H., Chanton, J. P., Morin, P., Rosenberry, D. O., Siegel, D. I., Ruud, O., ...
836 Reeve, A. S. (2004). Surface deformations as indicators of deep ebullition fluxes
837 in a large northern peatland. *GlobalBiogeochemicalCycles*, 18(1).
838 <https://doi.org/10.1029/2003GB002069>

839 Granberg, G., Ottosson-Löfvenius, M., Grip, H., Sundh, I., & Nilsson, M. (2001).
840 Effect of climatic variability from 1980 to 1997 on simulated methane emission
841 from a boreal mixed mire in northern Sweden. *GlobalBiogeochemicalCycles*,
842 15(4), 977–991. <https://doi.org/10.1029/2000GB001356>

843 Greinert, J., & Nützel, B. (2004). Hydroacoustic experiments to establish a method for
844 the determination of methane bubble fluxes at cold seeps. *GeoMarineLetters*,
845 24(2), 75–85. <https://doi.org/10.1007/s00367-003-0165-7>

846 Hamilton, S. (2007). *An analog electronics companion: basic circuit design for*
847 *engineers and scientists*. Cambridge University Press.

848 Hutchison, C. E. (1957). A treatise of limnology. Vol. 1 Geography, Physics and
849 chemistry. Wiley New York eNew York New York.

850 IPCC. (2007). *Climate change 2007: The physical science basis. Contribution of*
851 *Working Group I to the Fourth Assessment Report of the Intergovernmental*
852 *Panel on Climate Change*. (S. Solomon, Ed.) (Vol. 4). Cambridge University
853 Press, Cambridge, United Kingdom and New York, NY, USA.

854 IPCC. (2013). *Climate change 2013: The physical science basis. Contribution of*
855 *Working Group I to the Fifth Assessment Report of the Intergovernmental Panel*
856 *on Climate Change*. (T. F. Stocker, D. Qin, G.-K. Plattner, M. Tignor, S. K. Allen,

857 J. Boschung, ... P. M. Midgley, Eds.) (p. 1533). Cambridge University Press,
858 Cambridge, United Kingdom and New York, NY, USA.

859 Jain, A. K., & Juanes, R. (2009). Preferential Mode of gas invasion in sediments:
860 Grain-scale mechanistic model of coupled multiphase fluid flow and sediment
861 mechanics. *Journal Geophysical Research: Solid Earth*, 114(B8), B08101.
862 <https://doi.org/10.1029/2008JB006002>

863 Jones, S., Evans, G., & Galvin, K. (1999). Bubble nucleation from gas cavities—a
864 review. *Advances colloidInterfascience*, 80(1), 27–50.
865 [https://doi.org/10.1016/S0001-8686\(98\)00074-8](https://doi.org/10.1016/S0001-8686(98)00074-8)

866 Kellner, E., & Lundin, L.-C. (2001). Calibration of time domain reflectometry for
867 water content in peat soil. *HydrologyResearch*, 32(4-5), 315–332.
868 <https://doi.org/10.1029/WR026i010p02267>

869 Kettridge, N., & Binley, A. (2008). X-ray computed tomography of peat soils:
870 Measuring gas content and peat structure. *HydrologicalProcesses*, 22(25),
871 4827–4837. <https://doi.org/10.1002/hyp.7097>

872 Kettridge, N., & Binley, A. (2011). Characterization of peat structure using X-ray
873 computed tomography and its control on the ebullition of biogenic gas bubbles.
874 *Journal Geophysical Research: Biogeosciences*, 116(G1).
875 <https://doi.org/10.1029/2010JG001478>

876 Kirby, B. J. (2010). *Micro-and nanoscale fluid mechanics: transport in microfluidic*
877 *devices*. Cambridge University Press.

878 Li, X., & Yortsos, Y. (1995a). Theory of multiple bubble growth in porous media by

879 solute diffusion. *Chemical Engineering Science*, 50(8), 1247–1271.
880 [https://doi.org/10.1016/0009-2509\(95\)98839-7](https://doi.org/10.1016/0009-2509(95)98839-7)

881 Li, X., & Yortsos, Y. (1995b). Visualization and simulation of bubble growth in pore
882 networks. *AIChE Journal*, 41(2), 214–222. <https://doi.org/10.1002/aic.690410203>

883 Liu, L., Wilkinson, J., Koca, K., Buchmann, C., & Lorke, A. (2016). The role of
884 sediment structure in gas bubble storage and release. *Journal Geophysical
885 Research: Biogeosciences*, 121(7), 1992–2005.
886 <https://doi.org/10.1002/2016JG003456>

887 Marfunin, A. S. (2012). *Advanced Mineralogy: Volume 1 Composition, Structure, and
888 Properties of Mineral Matter: Concepts, Results, and Problems* (Vol. 1). Springer
889 Science & Business Media.

890 Martens, C. S., & Albert, D. B. (1994). Biogeochemical processes controlling gas
891 production, consumption, and transport in organic-rich marine sediments. In T. F.
892 Wever (Ed.), *Proceedings of the Gassy Mud Workshop. FWG, Kiel, Germany* (pp.
893 101–107).

894 Mustasaar, M., & Comas, X. (2017). Spatiotemporal variability in biogenic gas
895 dynamics in a subtropical peat soil at the laboratory scale is revealed using
896 high-resolution ground-penetrating radar. *Journal Geophysical Research:
897 Biogeosciences*, 122(9), 2219–2232. <https://doi.org/10.1002/2016JG003714>

898 Parsekian, A. D., Slater, L., & Giménez, D. (2012). Application of ground-penetrating
899 radar to measure near-saturation soil water content in peat soils.
900 *Water Resources Research*, 48(2). <https://doi.org/10.1029/2011WR011303>

901 von Post, L.. (1922). Swedish geological peat survey with the results obtained so far
902 (in Swedish). *SvenskaMosskulturföreningensTidskrift*, 36, 1–27.

903 Quinton, W. L., Hayashi, M., & Carey, S. K. (2008). Peat hydraulic conductivity in
904 cold regions and its relation to pore size and geometry. *HydrologicalProcesses*,
905 22(15), 2829–2837. <https://doi.org/10.1002/hyp.7027>

906 Quinton, W. L., Elliot, T., Price, J. S., Rezanezhad, F., & Heck, R. (2009). Measuring
907 physical and hydraulic properties of peat from X-ray tomography. *Geoderma*,
908 153(1), 269–277. <https://doi.org/10.1016/j.geoderma.2009.08.010>

909 Quinton, W. L., Gray, D. M., & Marsh, P. (2000). Subsurface drainage from
910 hummock-covered hillslopes in the Arctic tundra. *Journal Hydrology*, 237(1),
911 113–125. [https://doi.org/10.1016/S0022-1694\(00\)00304-8](https://doi.org/10.1016/S0022-1694(00)00304-8)

912 Ramirez, J. A., Baird, A. J., & Coulthard, T. J. (2016). The effect of pore structure on
913 ebullition from peat. *Journal Geophysical Research: Biogeosciences*, 121(6),
914 1646–1656. <https://doi.org/10.1002/2015JG003289>

915 Ramirez, J. A., Baird, A. J., Coulthard, T. J., & Waddington, J. M. (2015). Testing a
916 simple model of gas bubble dynamics in porous media. *WaterResourcesResearch*,
917 51(2), 1036–1049. <https://doi.org/10.1002/2014WR015898>

918 Rezanezhad, F., Quinton, W. L., Price, J. S., Elrick, D., Elliot, T. R., & Heck, R. J.
919 (2009). Examining the effect of pore size distribution and shape on flow through
920 unsaturated peat using computer tomography. *Hydrology Earth System Sciences*,
921 13, 1993–2002. <https://doi.org/10.5194/hess-13-1993-2009>

922 Richards, L. A. (1931). Capillary conduction of liquids through porous mediums.

923 *Physics*, 1(5), 318–333. <https://doi.org/10.1063/1.1745010>

924 Rosenberry, D. O., Glaser, P. H., & Siegel, D. I. (2006). The hydrology of northern
925 peatlands as affected by biogenic gas: current developments and research needs.
926 *Hydrological Processes*, 20(17), 3601–3610. <https://doi.org/10.1002/hyp.6377>

927 Rosenberry, D. O., Glaser, P. H., Siegel, D. I., & Weeks, E. P. (2003). Use of
928 hydraulic head to estimate volumetric gas content and ebullition flux in northern
929 peatlands. *Water Resources Research*, 39(3).
930 <https://doi.org/10.1029/2002WR001377>

931 Rothfuss, F., & Conrad, R. (1994). Development of a gas diffusion probe for the
932 determination of methane concentrations and diffusion characteristics in flooded
933 paddy soil. *FEMS microbiology Ecology*, 14(4), 307–318.

934 Shannon, R. D., White, J. R., Lawson, J. E., & Gilmour, B. S. (1996). Methane efflux
935 from emergent vegetation in peatlands. *Journal Ecology*, 239–246.
936 <https://doi.org/10.2307/2261359>

937 Terry, N., & Slater, L. (2017). Gas bubble size estimation in peat soils from EM wave
938 scattering observed with ground penetrating radar. *Water Resources Research*.
939 <https://doi.org/10.1002/2016WR019783>

940 Tokida, T., Miyazaki, T., & Mizoguchi, M. (2005). Ebullition of methane from peat
941 with falling atmospheric pressure. *Geophysical Research Letters*, 32(13).
942 <https://doi.org/10.1029/2005GL022949>

943 Topp, G. C., Davis, J., & Annan, A. P. (1980). Electromagnetic determination of soil
944 water content: Measurements in coaxial transmission lines.

945 *WaterresourcesResearch*, 16(3), 574–582.
946 <https://doi.org/10.1029/WR016i003p00574>

947 Walter, B. P., & Heimann, M. (2000). A process-based, climate-sensitive model to
948 derive methane emissions from natural wetlands: Application to five wetland sites,
949 sensitivity to model parameters, and climate. *GlobalBiogeochemicalCycles*, 14(3),
950 745–765. <https://doi.org/10.1029/1999GB001204>

951 Walter, B. P., Heimann, M., Shannon, R. D., & White, J. R. (1996). A process-based
952 model to derive methane emissions from natural wetlands.
953 *GeophysicalResearchLetters*, 23(25), 3731–3734.
954 <https://doi.org/10.1029/96GL03577>

955 Wright, W., & Comas, X. (2016). Estimating methane gas production in peat soils of
956 the Florida Everglades using hydrogeophysical methods. *Journal Geophysical*
957 *Research: Biogeosciences*, 121(4), 1190–1202.
958 <https://doi.org/10.1002/2015JG003246>

959 Yortsos, Y. C., & Parlari, M. (1989). Phase change in binary systems in porous media:
960 application to solution-gas drive. In *SPE annual technical conference and*
961 *exhibition*. Society of Petroleum Engineers.
962 <https://doi.org/10.2118/19697-MS>

963 Yousfi, E., Zarcone, C., Bories, S., & Lenormand, R. (1990). Liberation of Solution
964 Gas during Pressure Depletion in a 2-Dimensional Porous Medium.
965 *IFPResearchConf.,Arles,France*.

966 Yu, C., Warrick, A., & Conklin, M. (1999). Derived functions of time domain

967 reflectometry for soil moisture measurement. *WaterResourcesResearch*, 35(6),

968 1789–1796. <https://doi.org/10.1029/1999WR900025>

969

970

971

972

973

974

975

976

977

978

979

980

981

982

983

984

985

986

987

988

989 **List of the table captions:**

990 **Table 1.** Analogous parameters in the general capacitance model.

991 **Table 2.** Decreases in hydrostatic pressure (average = 4.1 cm, standard error = 3.6 cm)
992 and corresponding increases in CH₄ concentrations (average = 252.8 mmol m⁻³,
993 standard error = 180.1 mmol m⁻³) during Stage II.

994 **Table 3.** Structural parameters of each layer.

995

996 **List of the figure captions:**

997 **Figure 1.** Conceptual model of accumulation of CH₄-enriched gas bubbles. a-c)
998 Heterogeneous nucleation bubble clusters move from specific nucleation sites to the
999 upper layers (Li & Yortsos, 1995b; Yousfi et al., 1990). d) Analogy between dielectric
1000 polarization of a capacitor and bubble entrapment in a pore throat (upward is defined
1001 as positive direction). e) Lumped capacitance model for bubble storage. D_i , d_i , C_i , R_i ,
1002 $\Delta \Psi_{Ti}$ and $\Delta \Psi_{Ci}$ represent the depth referenced to the water surface, thickness,
1003 capacitance, resistance, potential difference of the capacitor and potential difference
1004 of energy source of the i th layer, respectively.

1005 **Figure 2.** Zone I, II and III represent (I) the range of regular water retention, (II)
1006 charging of biogenic bubbles, and (III) the over-pressured condition with the highly
1007 uncertain possibility of breaking down the capacitor, respectively.

1008 **Figure 3.** a) Map showing the experimental sites; b) Laboratory installation. L , W and
1009 H are the length, width and height of the sample, respectively; D_i is distance between
1010 the i th scanning line and water table; d and l are the vertical scanning interval and

1011 horizontal interval, respectively; Δt_{em} is the two-way travel time of the
1012 electromagnetic signal through the sample monolith measured with a ground
1013 penetrating radar (GPR) device; c) Resin-impregnated peat sections.

1014 **Figure 4.** Relative permittivity, estimated water content and changes in gas contents
1015 with GPR scanning on Day 2, 18, 40, 53, 68, 89, 102 during Stage I and III of the
1016 observation period. The changes in water contents between the initial state and end
1017 state were used to estimate gas contents, and thereby gas capacitance.

1018 **Figure 5.** Result of changes in gas content. a) Layer-averaged increases in gas
1019 contents on Day 18, 40, 53, 68, 89, 102 during the observation period. b) Bulk
1020 averaged gas contents during the observation period. c) Bubble capacitances of each
1021 depth.

1022 **Figure 6.** Results of estimated long-term changes in gas content at four depths: a)
1023 Time-lapse layer-averaged relative permittivity based on GPR measurement. The
1024 value of each layer represents the average of 12 traces at corresponding depth, b) area
1025 percentage of gas bubbles hand-drawn from scanning images.

1026 **Figure 7.** Power spectra associated with GPR scanning at sampling points P2 and P3.
1027 P3 exhibits frequency shifts over the whole period whilst P2 shows a more constant
1028 attenuation pattern, suggesting that scattering responses at P2 and P3 are Mie and
1029 Rayleigh type, respectively.

1030 **Figure 8.** Vertical variation in peat structure: a) values of void ratio r_1 , bubble
1031 capacitance C_i , von Post humification and corresponding photos at different depths. b)
1032 A sample slice of X-ray CT Scanning of peat section and the corresponding histogram

1033 of voxel intensity; c) Histograms of voxel intensity of 18 sections of the peat sample
1034 showing the volume contrast between resin-filled pore space (r1) and peat particles
1035 (r2).

1036

1037

1038

1039

1040

1041

1042

1043

1044

1045

1046

1047

1048

1049

1050

1051

1052

1053

1054

1055 **Tables**

1056 **Table 1.** Analogous parameters in the general capacitance model

		Applications		
		Electric charge storage	Soil water storage	Biogenic gas bubble storage in shallow peat
Stored property	Electrical charge		Water in soil pores	Biogenic CH ₄ -enriched gas bubbles
Stored amount	Stored electric charge Q		Volumetric content of pore water	Volumetric content of gas bubbles θ_g
Power source	$\Delta\psi_T$ Voltage (Electric potential difference)		Hydraulic potential difference	Buoyancy
Potential difference at equilibrium	$\Delta\psi_C$ Induced potential difference between the two terminals of the dielectric medium		Capillary potential against out flow of pore water	Capillary potential holding gas bubbles against buoyancy effect
Capacitance C	Electrical capacitance		(Water) Capillary capacitance	Bubble capacitance

1057

1058

1059

1060

1061 **Table 2.** Decreases in hydrostatic pressure (average = 4.1 cm, standard error = 3.6 cm)

1062 and corresponding increases in CH₄ concentrations (average = 252.8 mmol m⁻³,

1063 standard error = 180.1 mmol m⁻³) during Stage II.

Events	Average decreases in hydrostatic pressure (cm)	Increases in CH ₄ concentration (mmol m ⁻³)
1	2.0	213.6
2	3.3	363.3
3	2.6	93.5
4	10.4	505.0
5	2.1	88.4
Average	4.1	252.8
Standard error	3.6	180.1

1064

1065

1066

1067

1068

1069

1070

1071

1072

1073

1074

1075

1076

1077 **Table 3.** Structural parameters of each layer

Layer i	Depth (cm)	von Post Humification
1	0 – 5	H2 – H3
2	5 – 10	H2
3	10 – 15	H3
4	15 – 20	H4
5	20 – 25	H5

1078

1079

1080

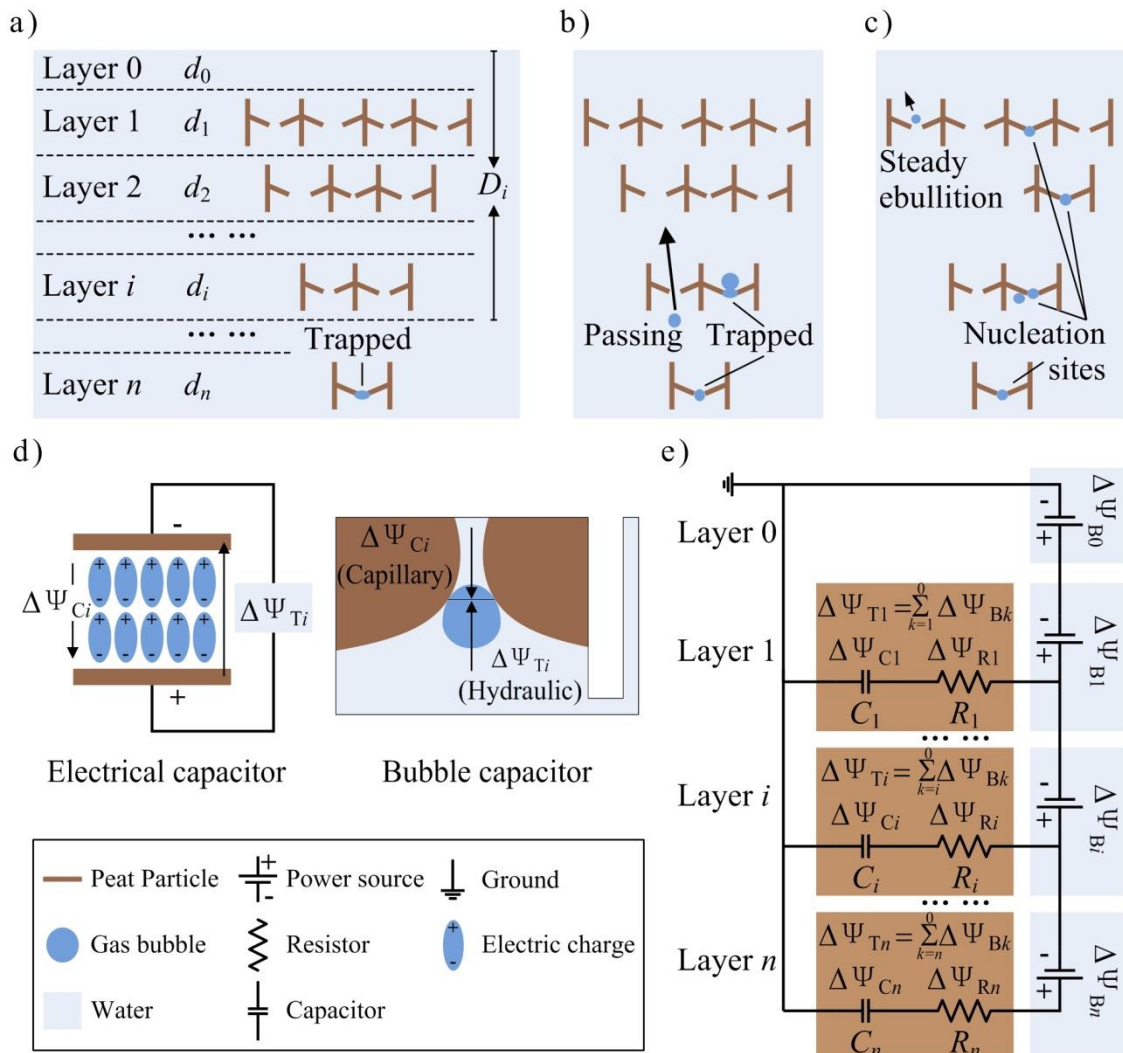
1081

1082

1083

1084

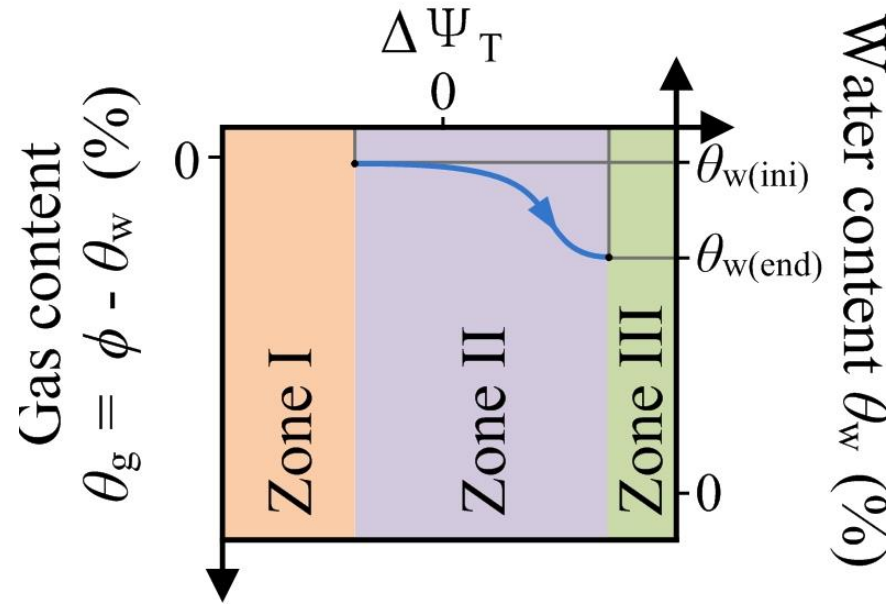
1085 **Figures**



1087

1088 **Figure 1.** Conceptual model of accumulation of CH₄-enriched gas bubbles. a-c)
 1089 Heterogeneous nucleation bubble clusters move from specific nucleation sites to the
 1090 upper layers (Li & Yortsos, 1995b; Yousfi et al., 1990). d) Analogy between dielectric
 1091 polarization of a capacitor and bubble entrapment in a pore throat (upward is defined
 1092 as positive direction). e) Lumped capacitance model for bubble storage. D_i , d_i , C_i , R_i ,
 1093 $\Delta \Psi_{Ti}$ and $\Delta \Psi_{Ci}$ represent the depth referenced to the water surface, thickness,
 1094 capacitance, resistance, potential difference of the capacitor and potential difference
 1095 of energy source of the i th layer, respectively.

1096



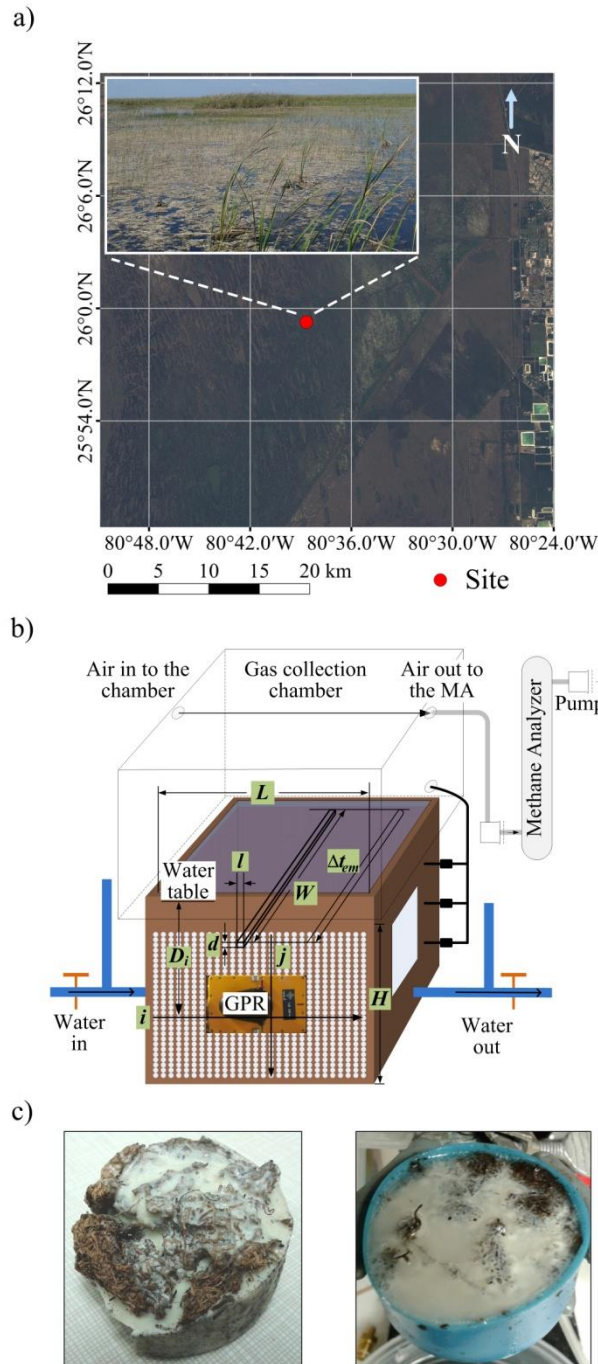
1097

1098 **Figure 2.** Zone I, II and III represent (I) the range of regular water retention, (II) charging of biogenic bubbles, and (III) the over-pressured

1099 condition with the highly uncertain possibility of breaking down the capacitor, respectively.

1100

1101



1102

1103 **Figure 3.** a) Map showing the experimental sites; b) Laboratory installation. L , W and

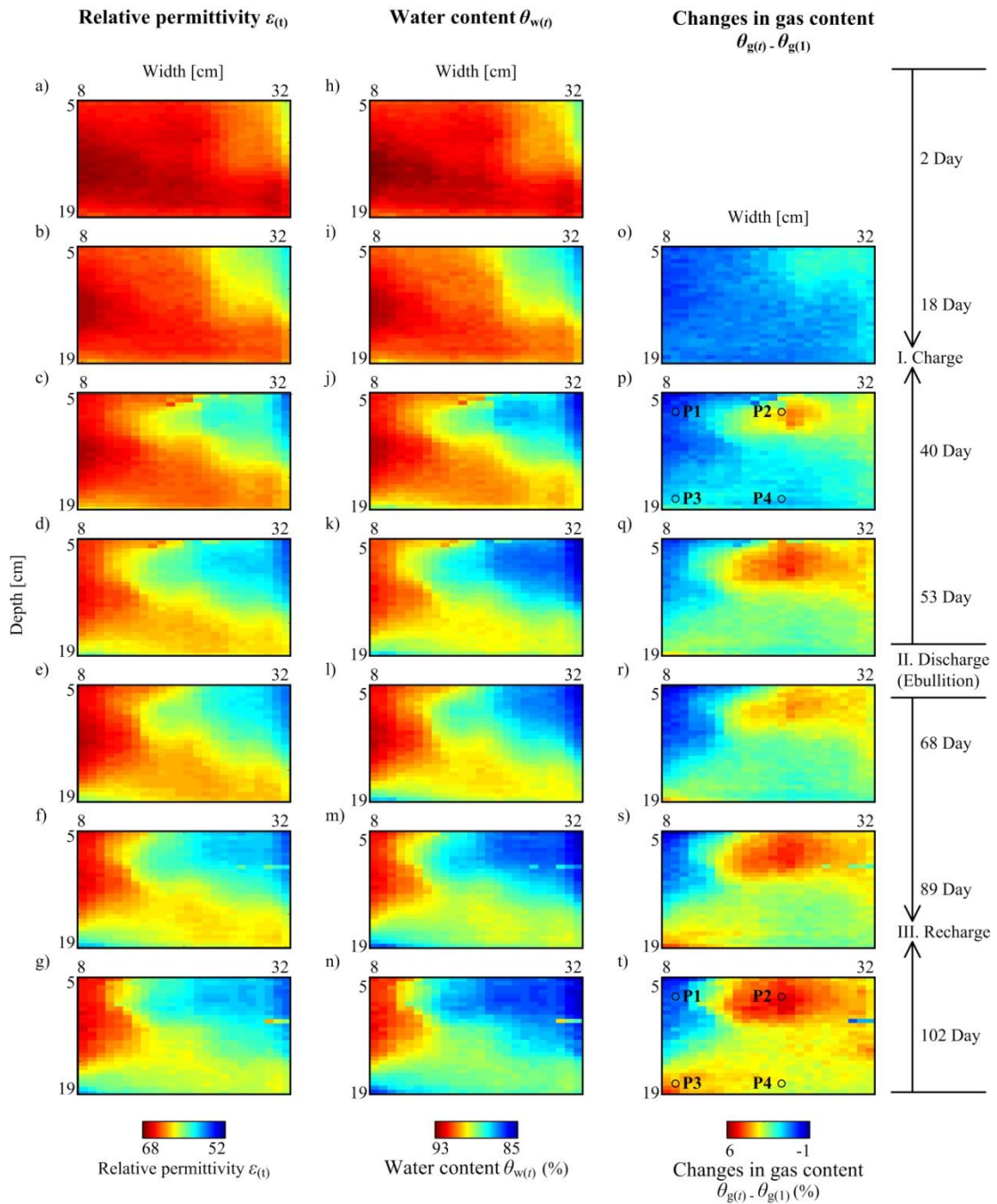
1104 H are the length, width and height of the sample, respectively; D_i is distance between

1105 the i th scanning line and water table; d and l are the vertical scanning interval and

1106 horizontal interval, respectively; Δt_{em} is the two-way travel time of the

1107 electromagnetic signal through the sample monolith measured with a ground

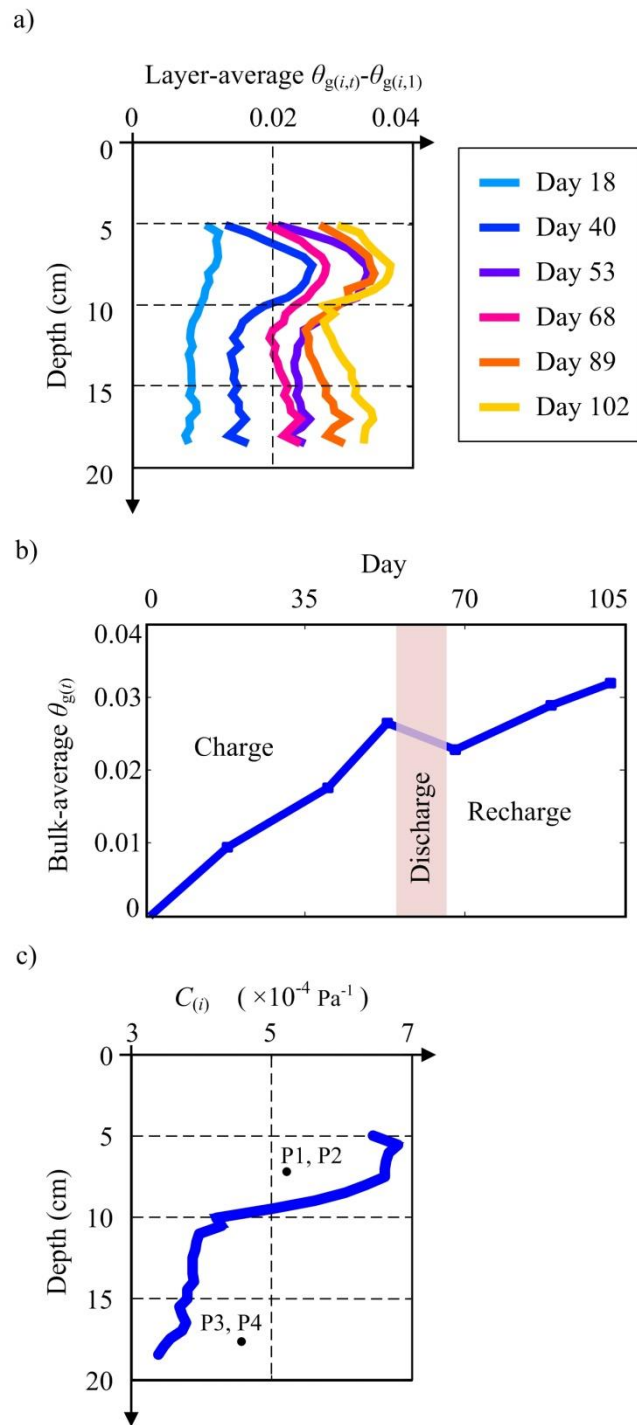
1108 penetrating radar (GPR) device; c) Resin-impregnated peat sections.



1110

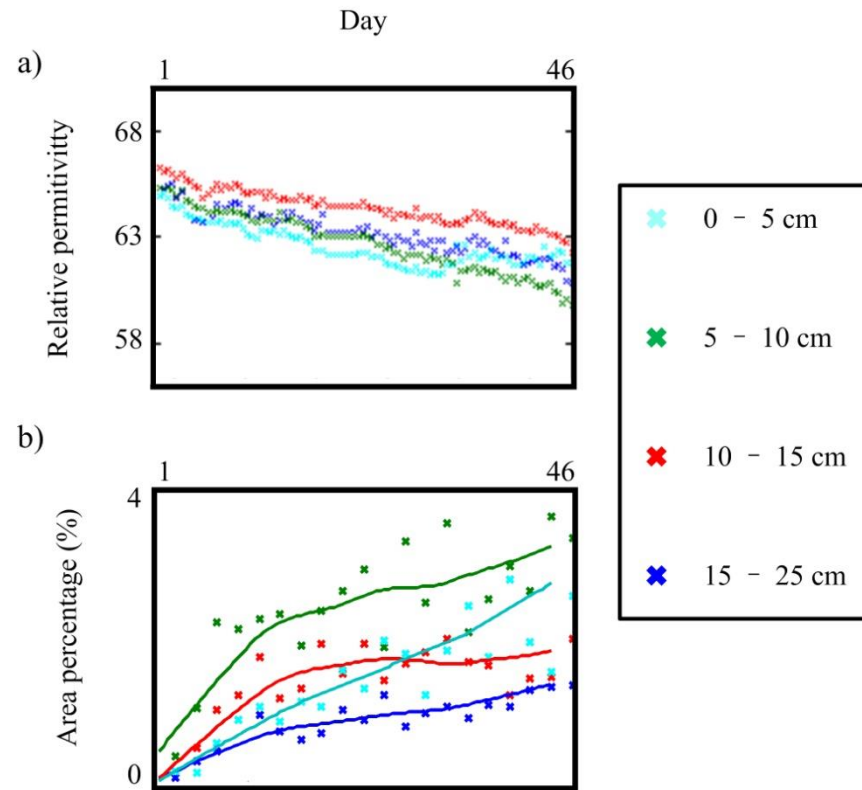
1111 **Figure 4.** Relative permittivity, estimated water content and changes in gas contents
 1112 with GPR scanning on Day 2, 18, 40, 53, 68, 89, 102 during Stage I and III of the
 1113 observation period. The changes in water contents between the initial state and end
 1114 state were used to estimate gas contents, and thereby gas capacitance.

1115



1117

1118 **Figure 5.** Result of changes in gas content. a) Layer-averaged increases in gas
 1119 contents on Day 18, 40, 53, 68, 89, 102 during the observation period. b) Bulk
 1120 averaged gas contents during the observation period. c) Bubble capacitances of each
 1121 depth.



1122

1123 **Figure 6.** Results of estimated long-term changes in gas content at four depths: a) Time-lapse layer-averaged relative permittivity based on GPR

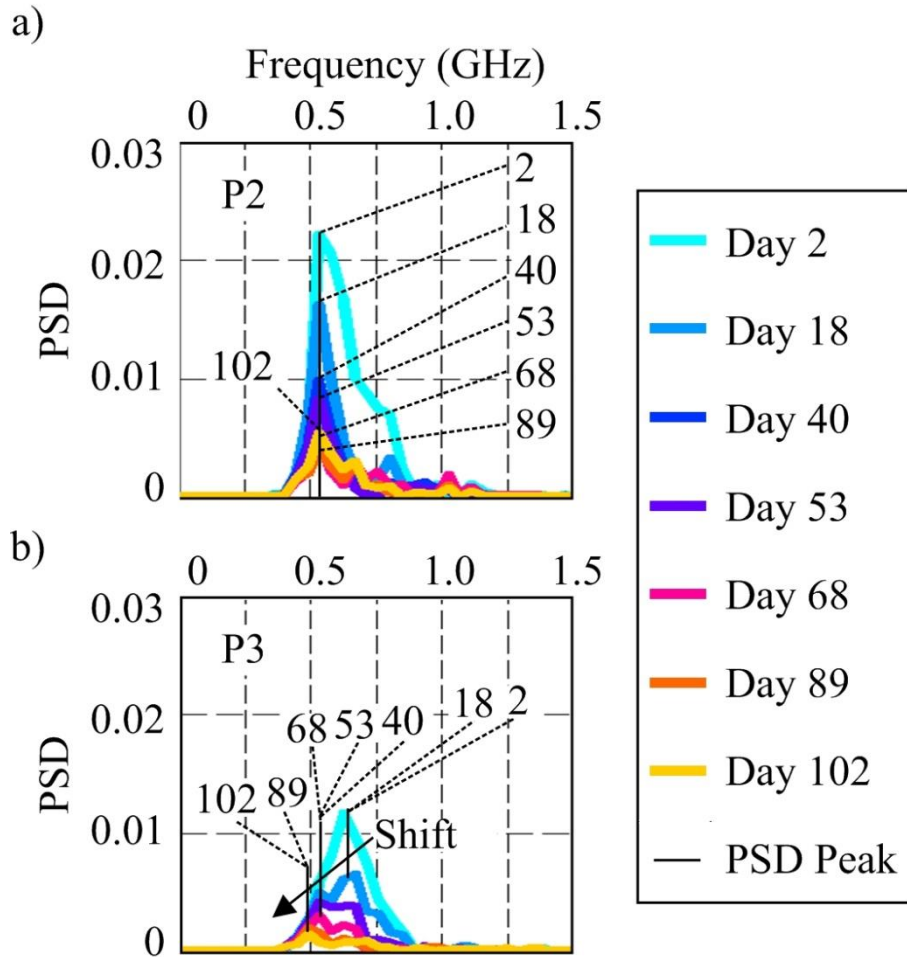
1124 measurement. The value of each layer represents the average of 12 traces at corresponding depth, b) area percentage of gas bubbles hand-drawn

1125 from scanning images.

1126

1127

1128



1129

1130 **Figure 7.** Power spectra associated with GPR scanning at sampling points P2 and P3.

1131 P3 exhibits frequency shifts over the whole period whilst P2 shows a more constant

1132 attenuation pattern, suggesting that scattering responses at P2 and P3 are Mie and

1133 Rayleigh type, respectively.

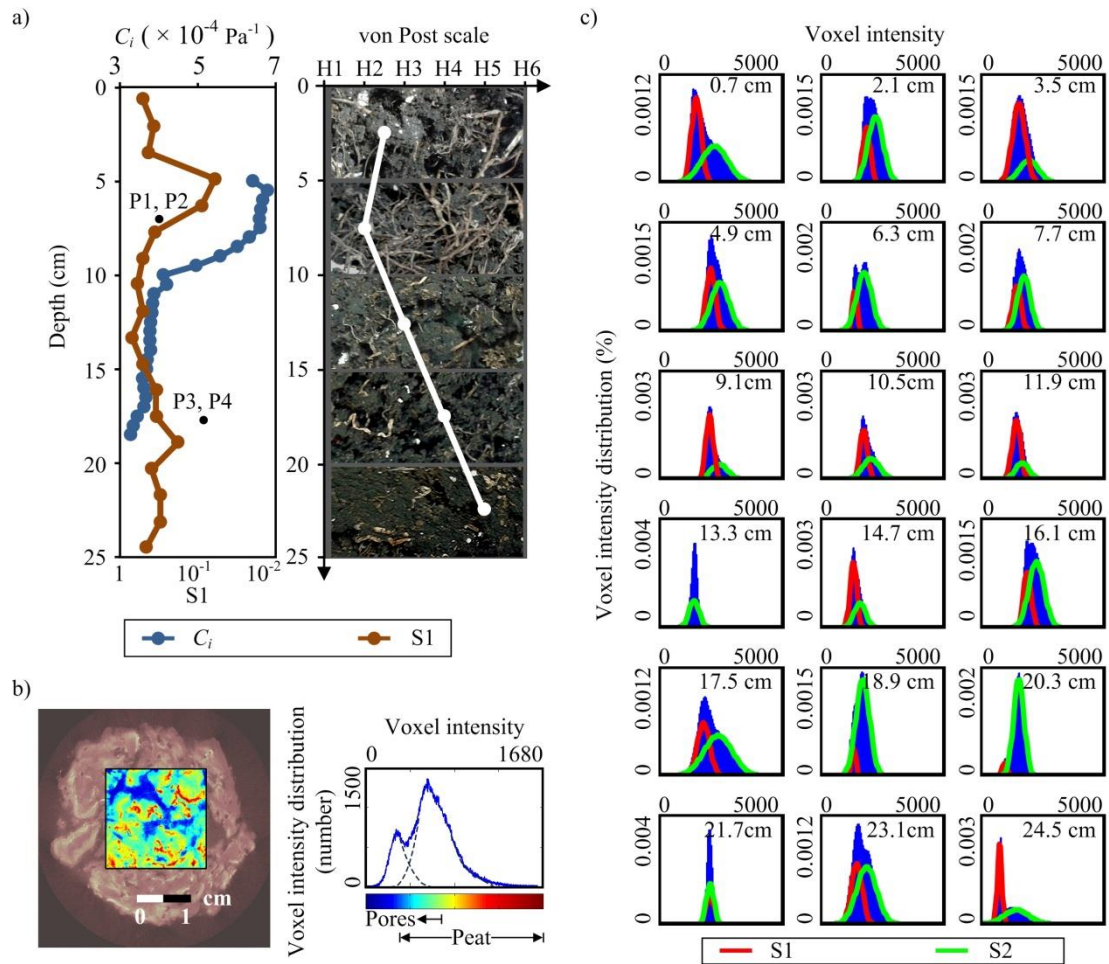
1134

1135

1136

1137

1138



1139

1140 **Figure 8.** Vertical variation in peat structure: a) values of void ratio r_1 , bubble

1141 capacitance C_i , von Post humification and corresponding photos at different depths. b)

1142 A sample slice of X-ray CT Scanning of peat section and the corresponding histogram

1143 of voxel intensity; c) Histograms of voxel intensity of 18 sections of the peat sample

1144 showing the volume contrast between resin-filled pore space (r_1) and peat particles

1145 (r_2).

1146

1147

Figure 1.

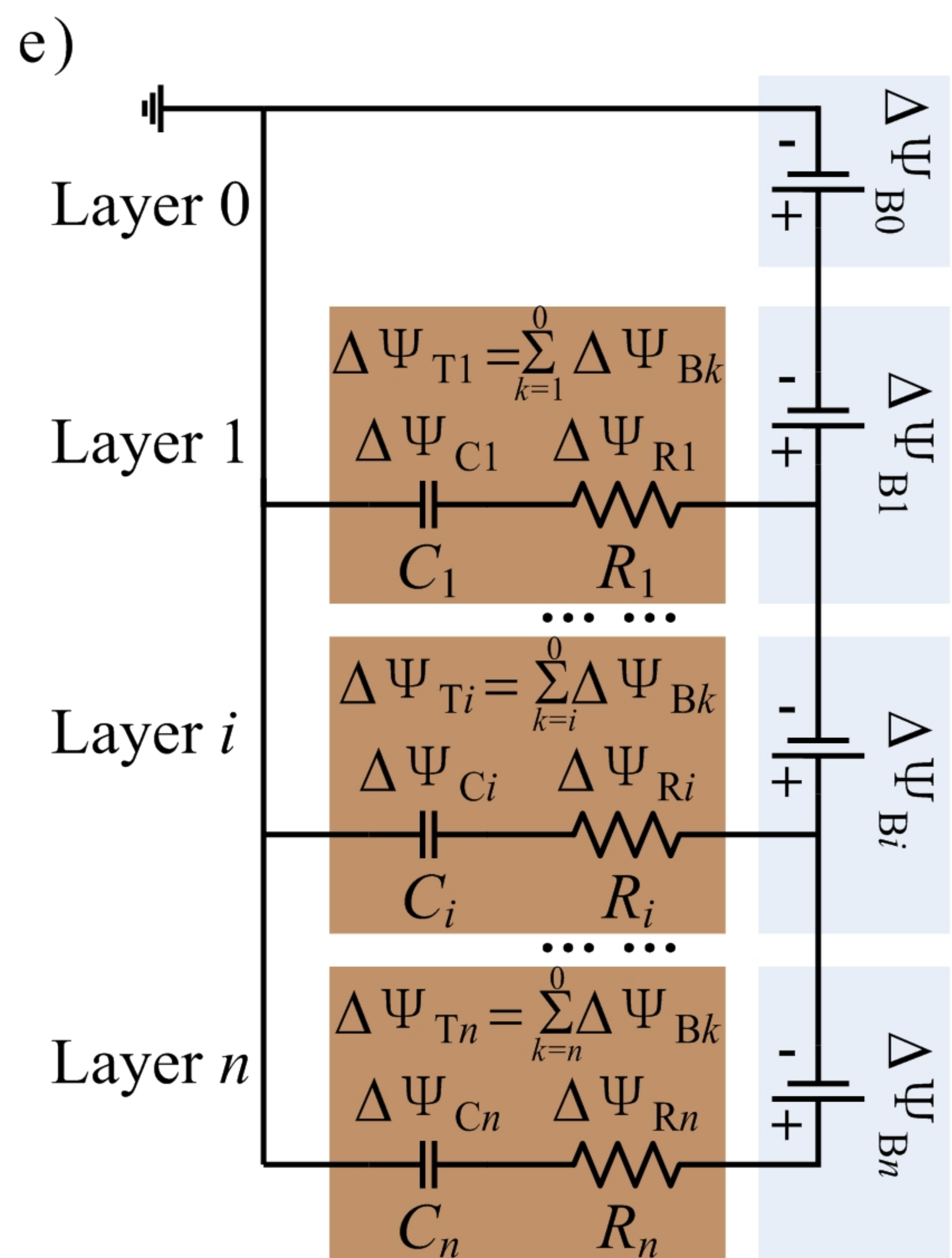
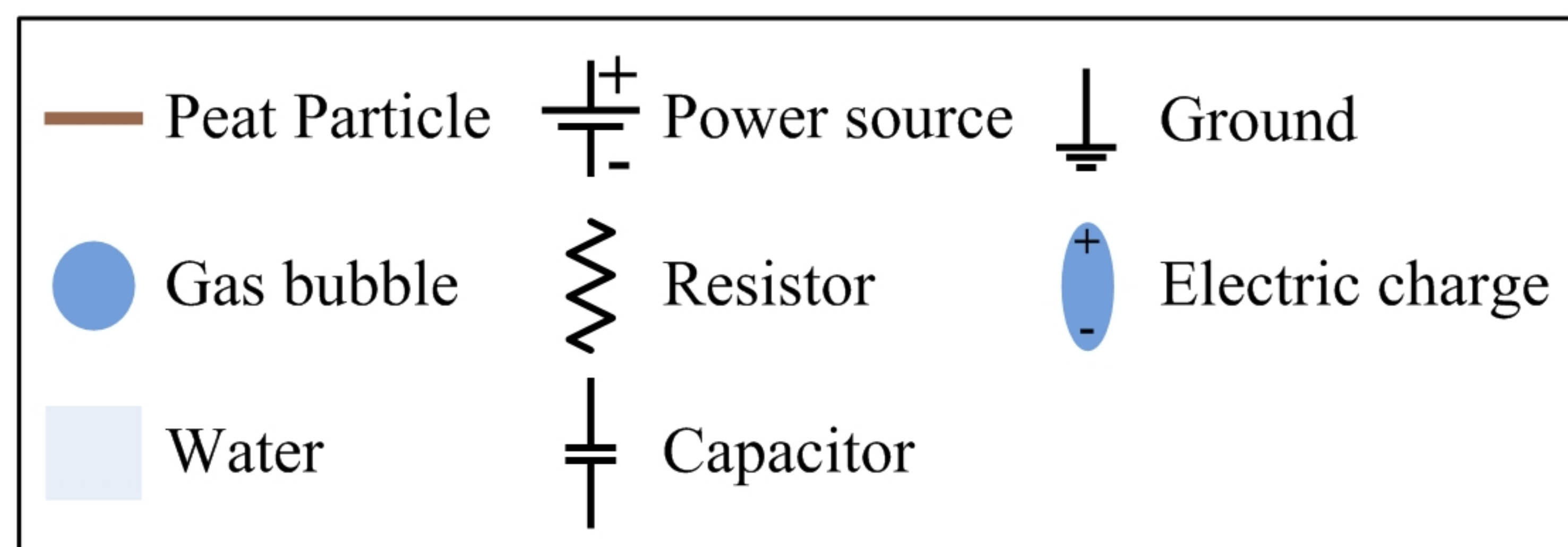
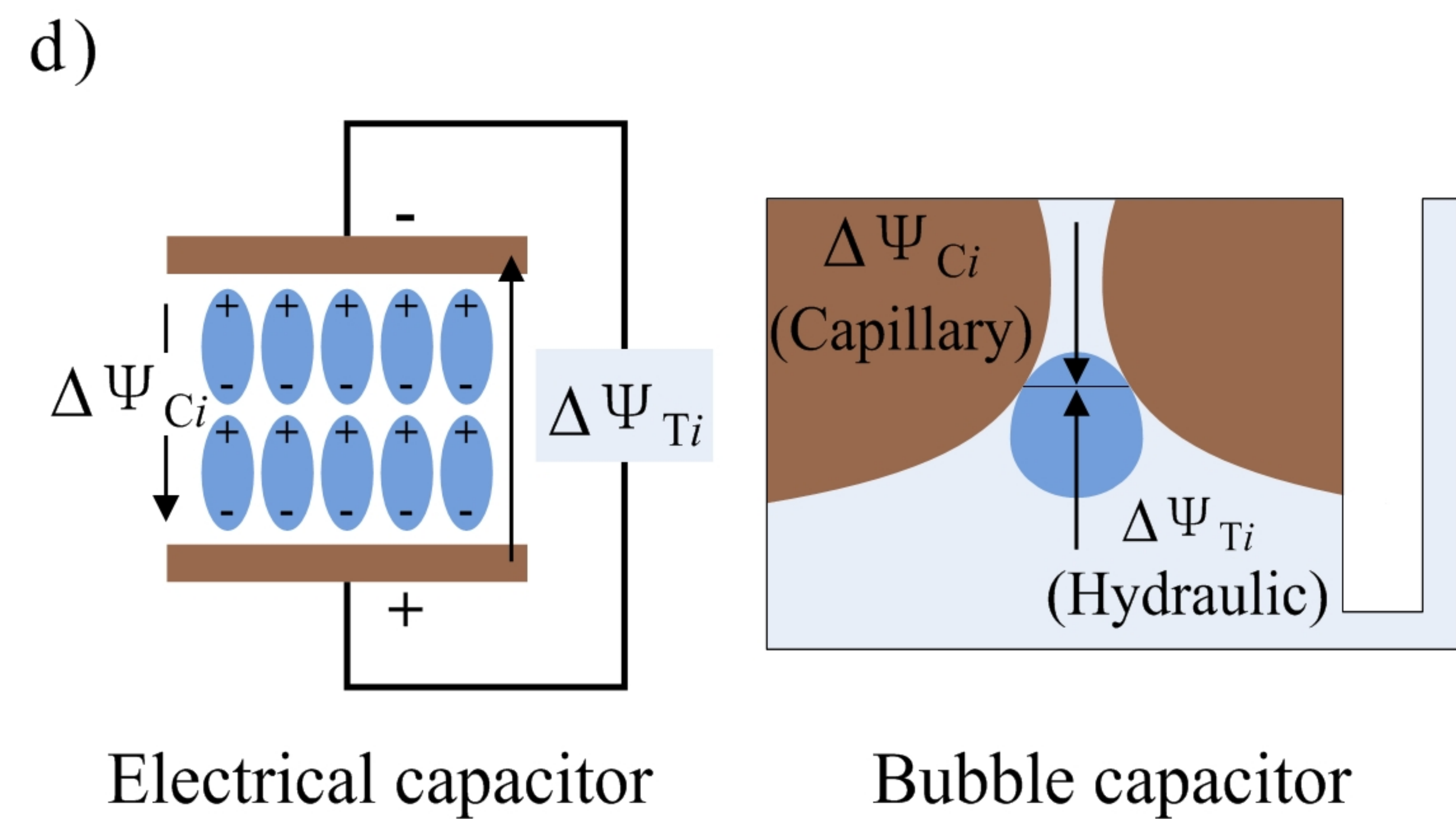
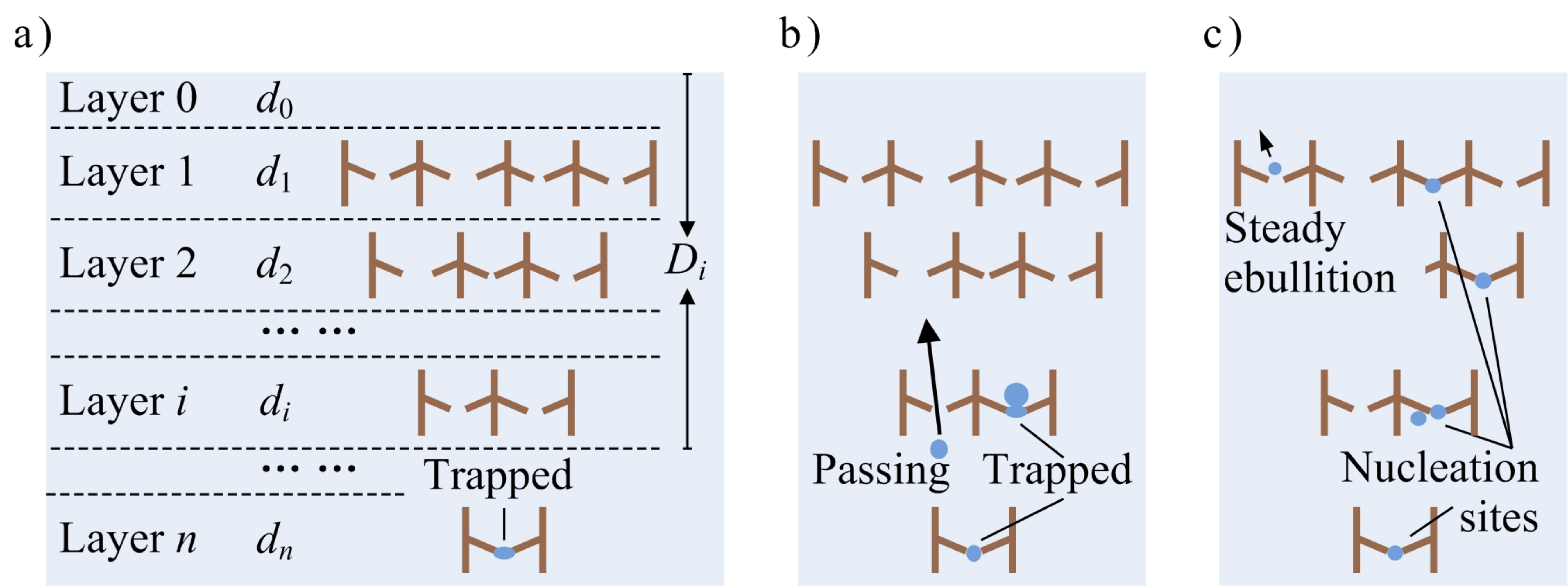
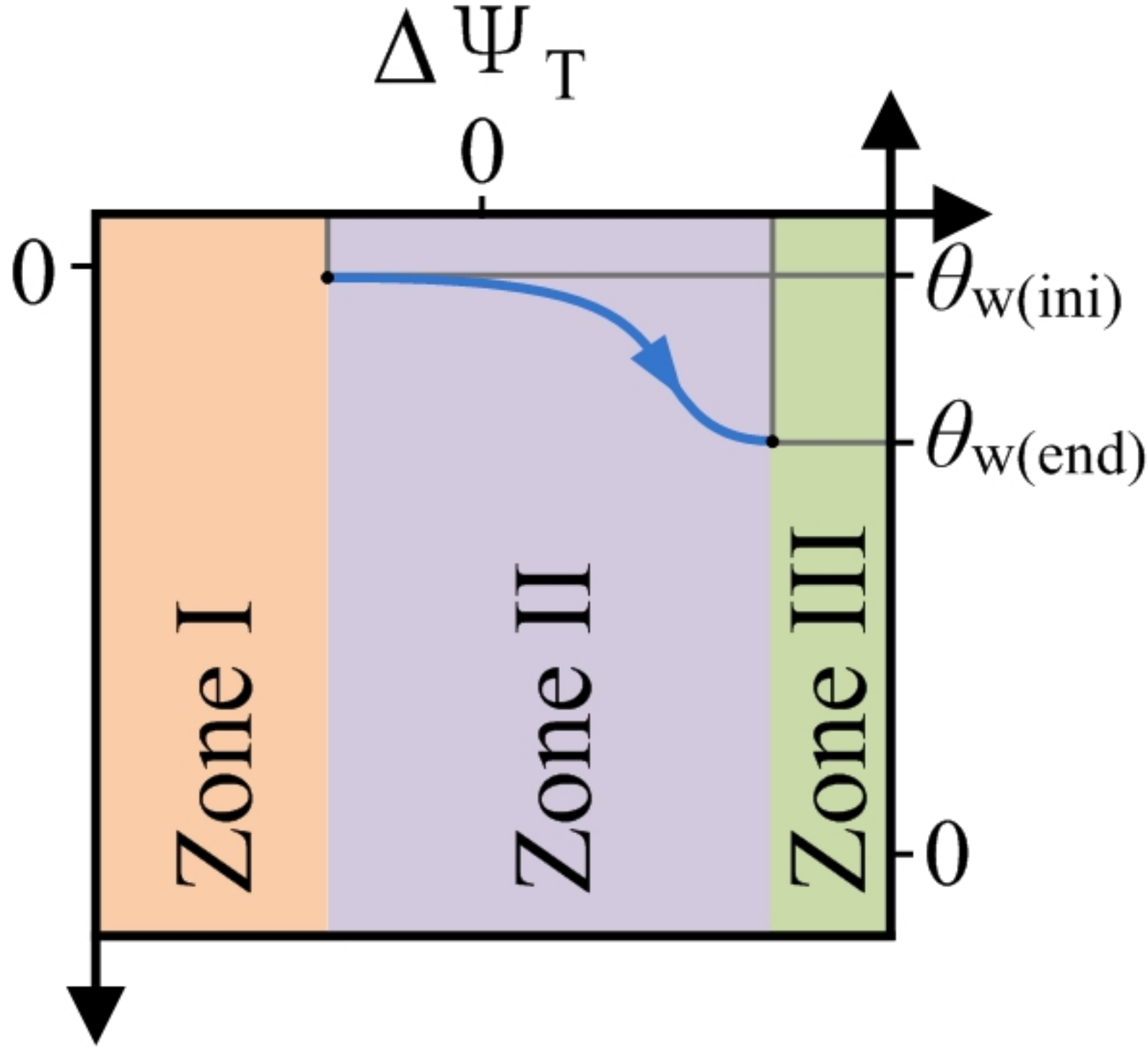


Figure 2.

Gas content

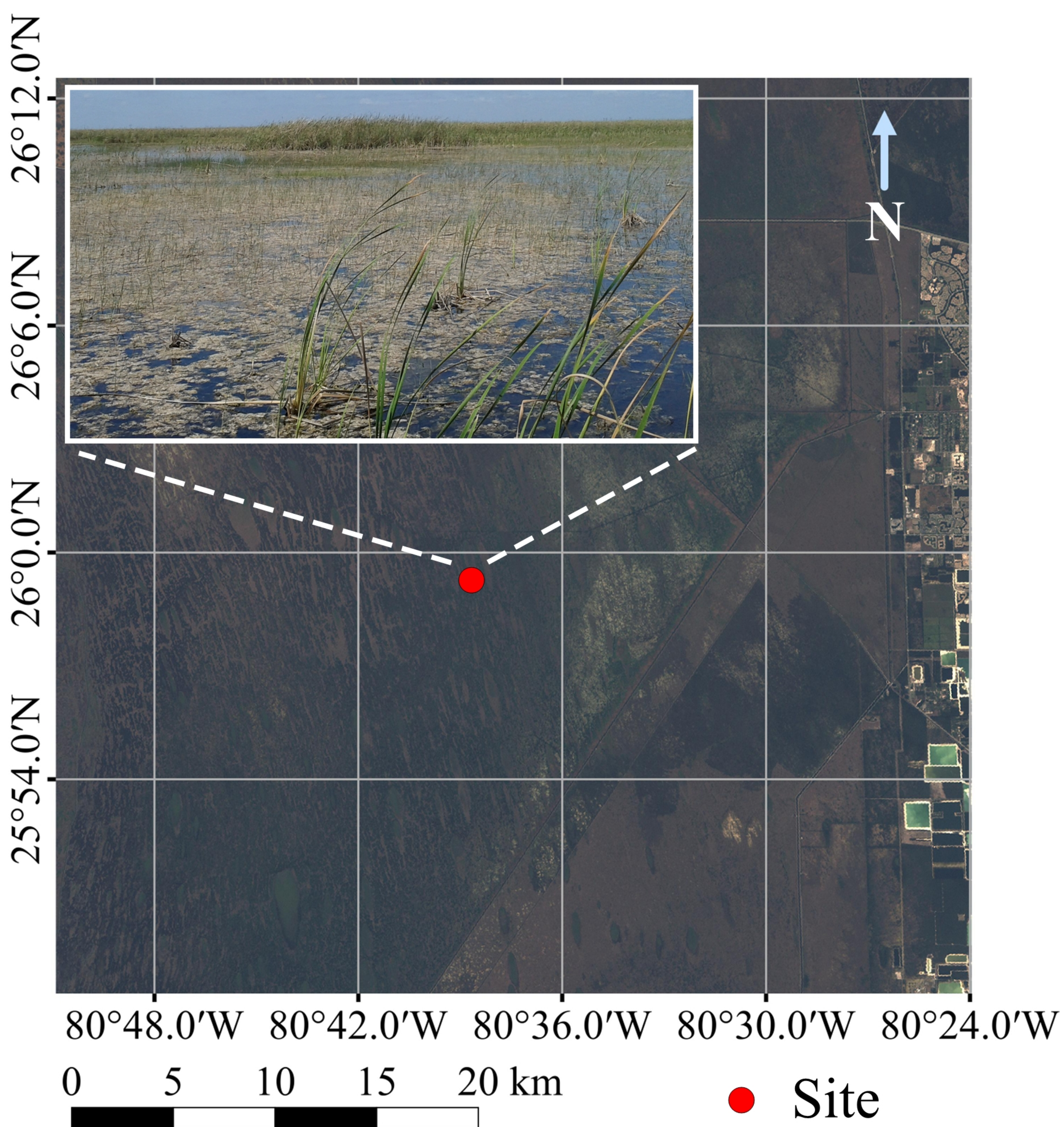
$$\theta_g = \phi - \theta_w \quad (\%)$$



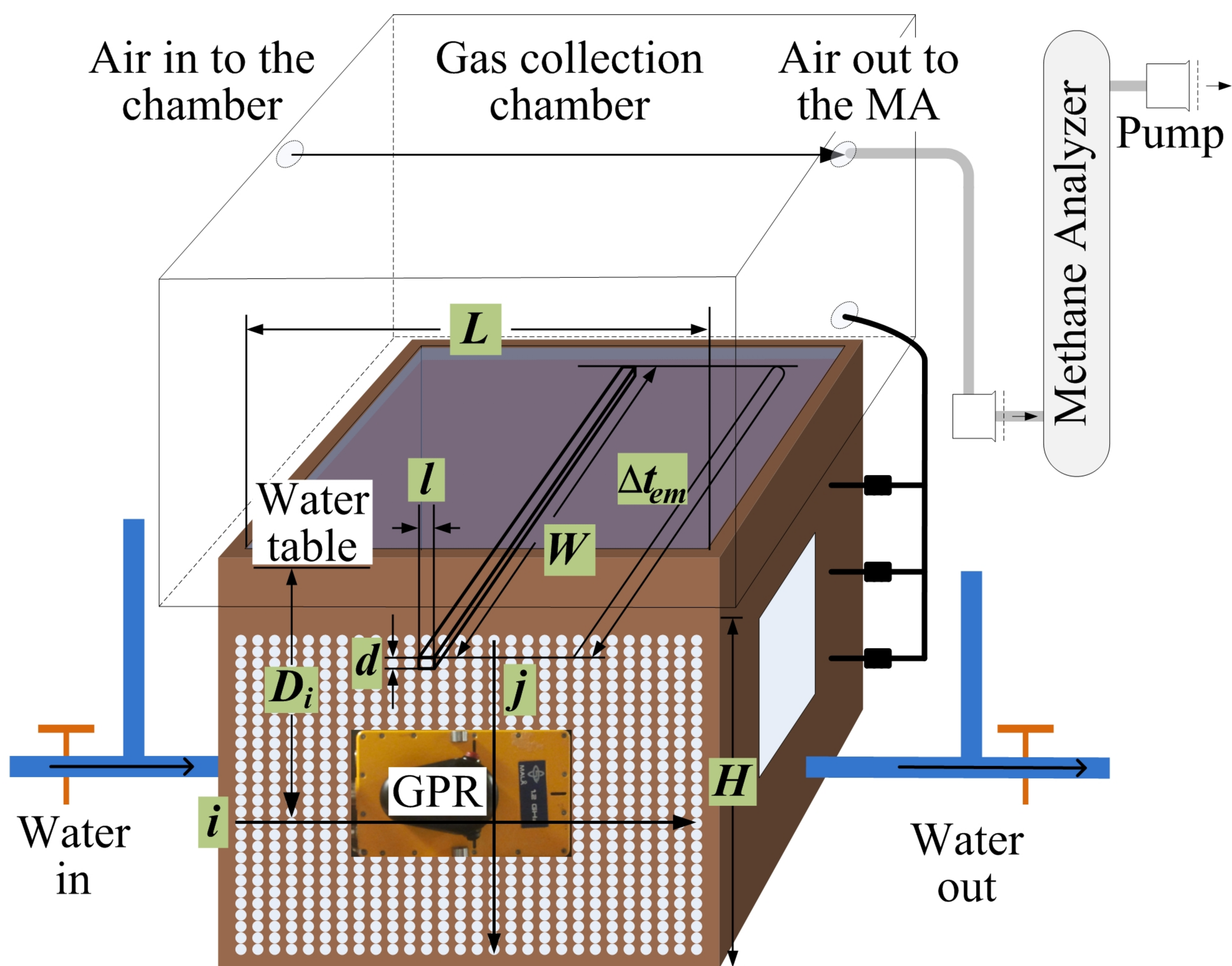
Water content θ_w (%)

Figure 3.

a)



b)



c)



Figure 4.

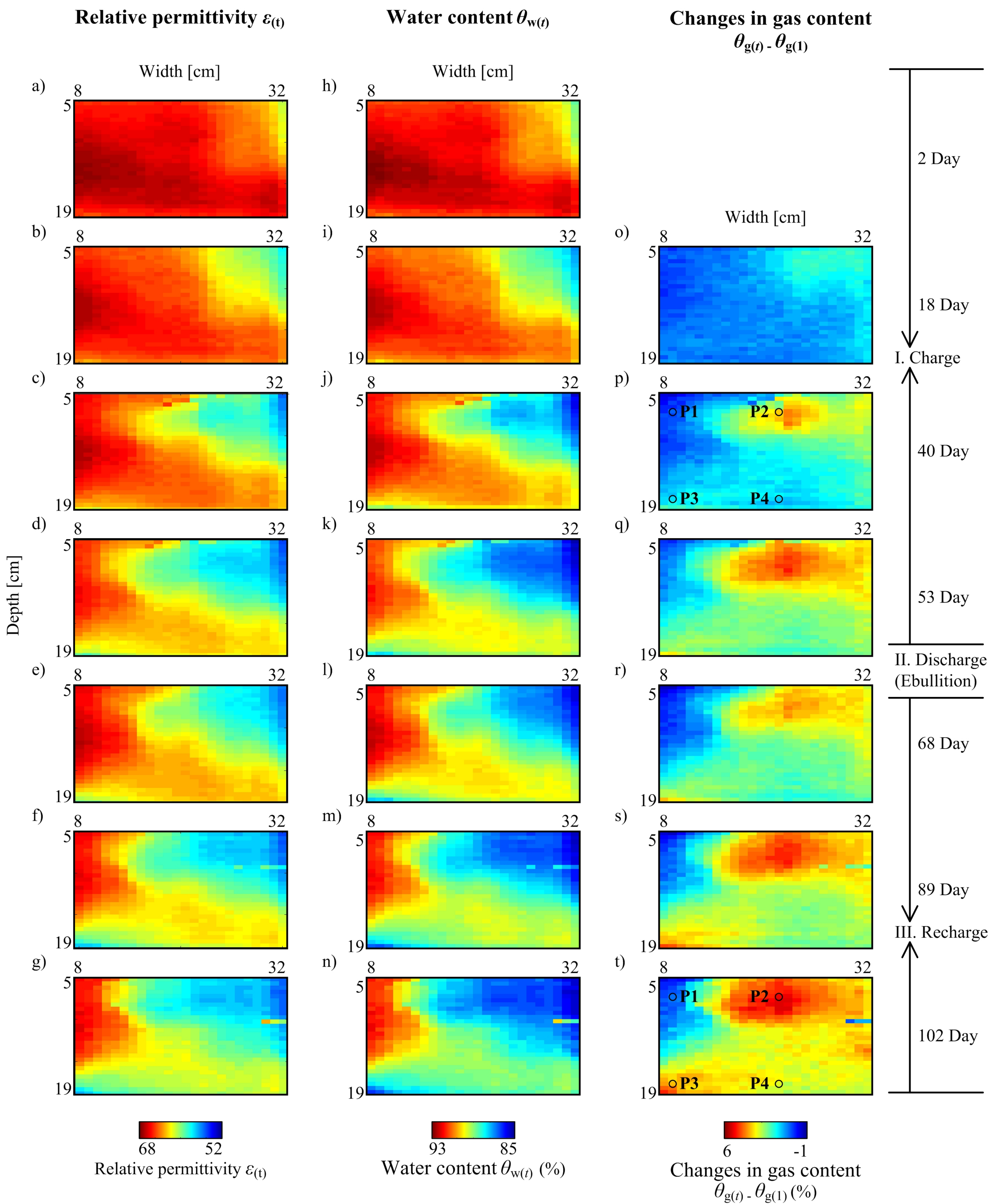
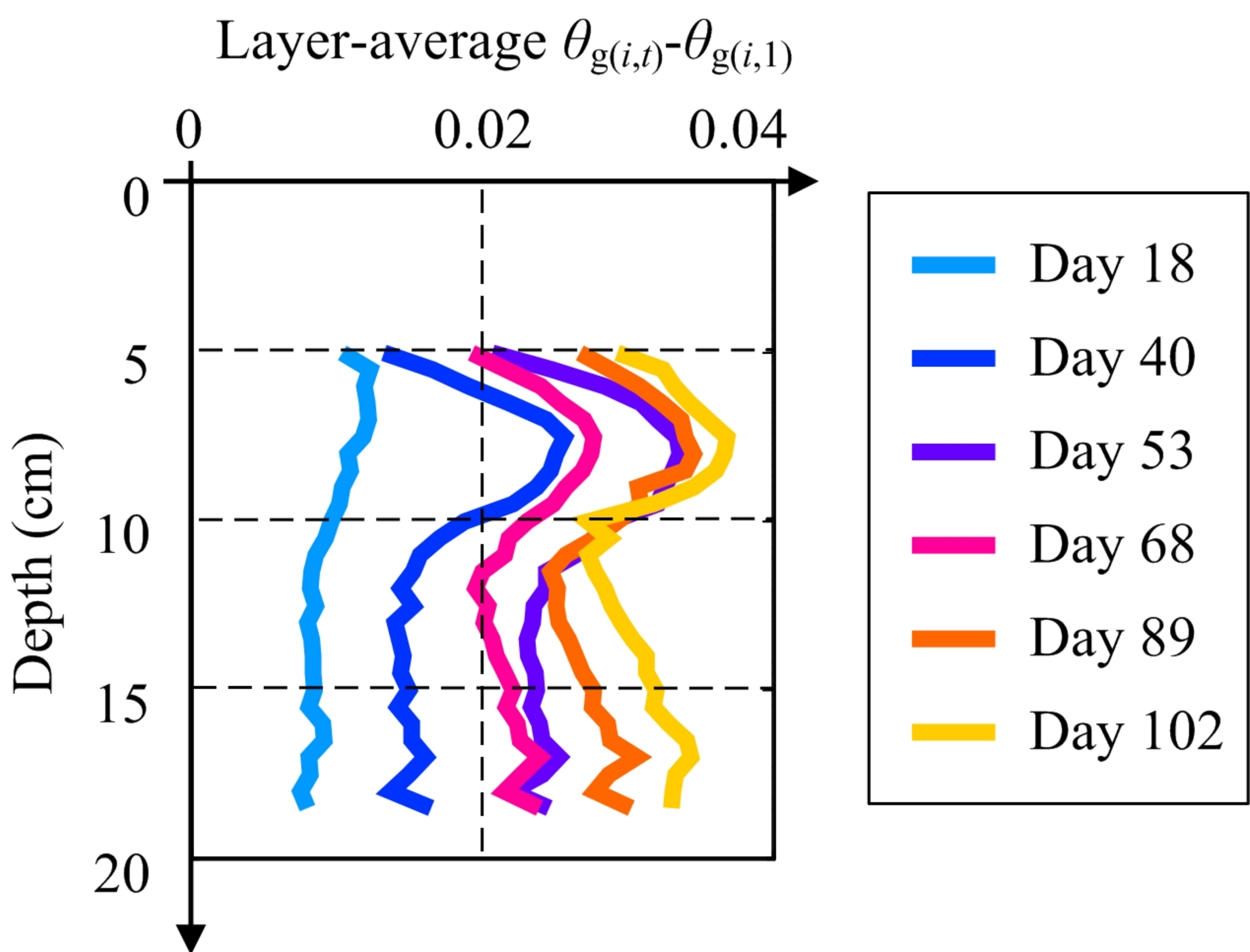
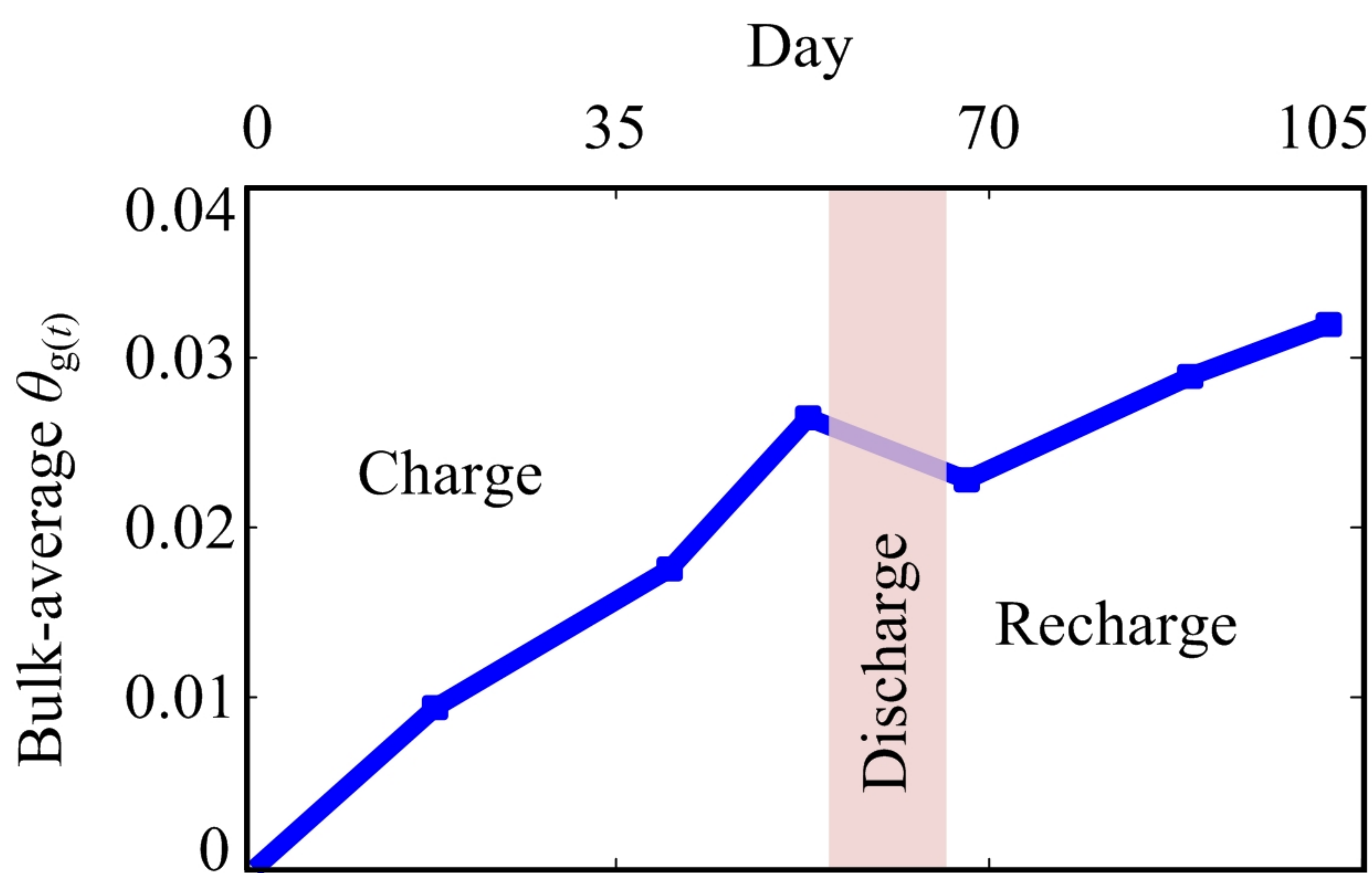


Figure 5.

a)



b)



c)

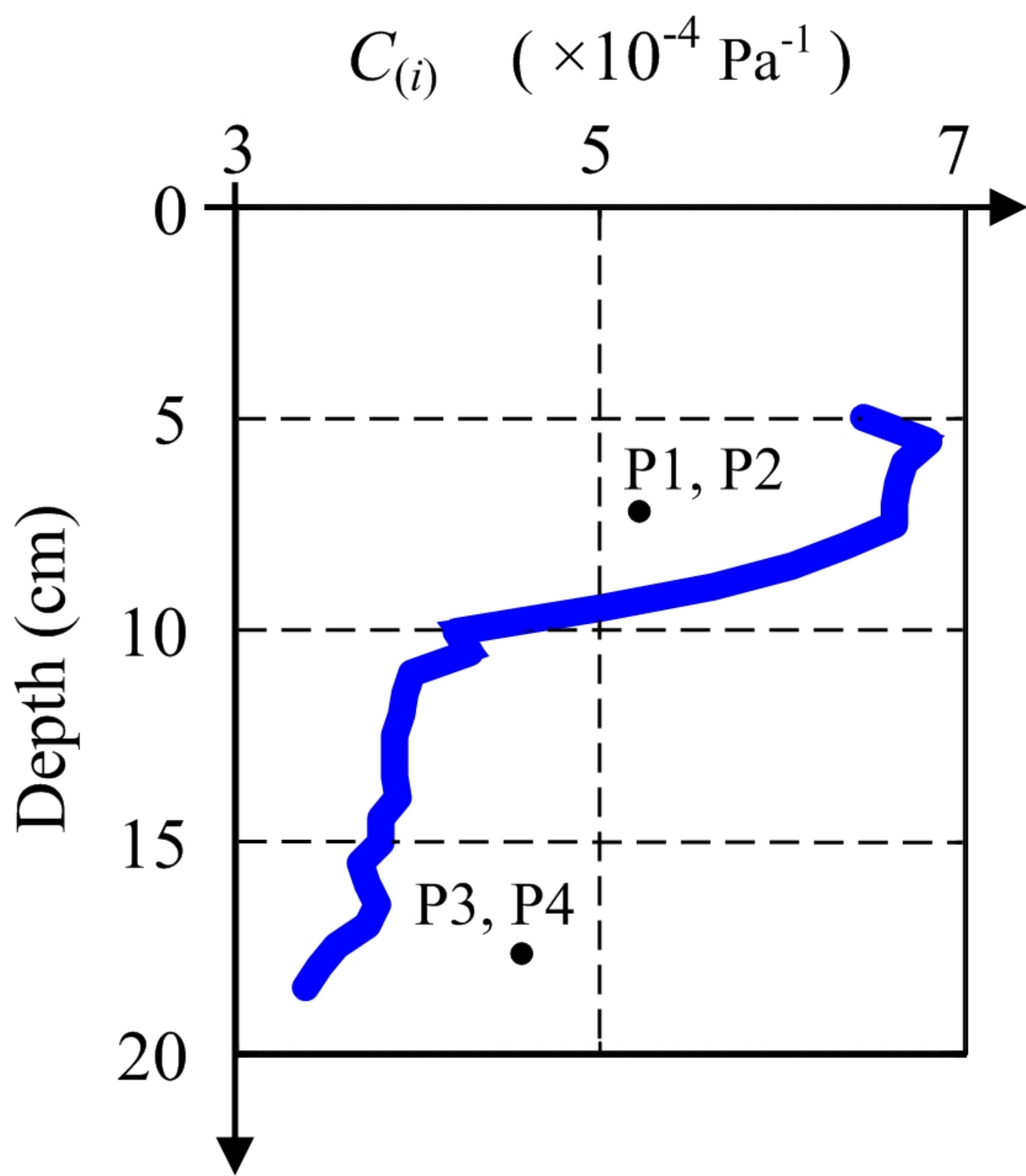


Figure 6.

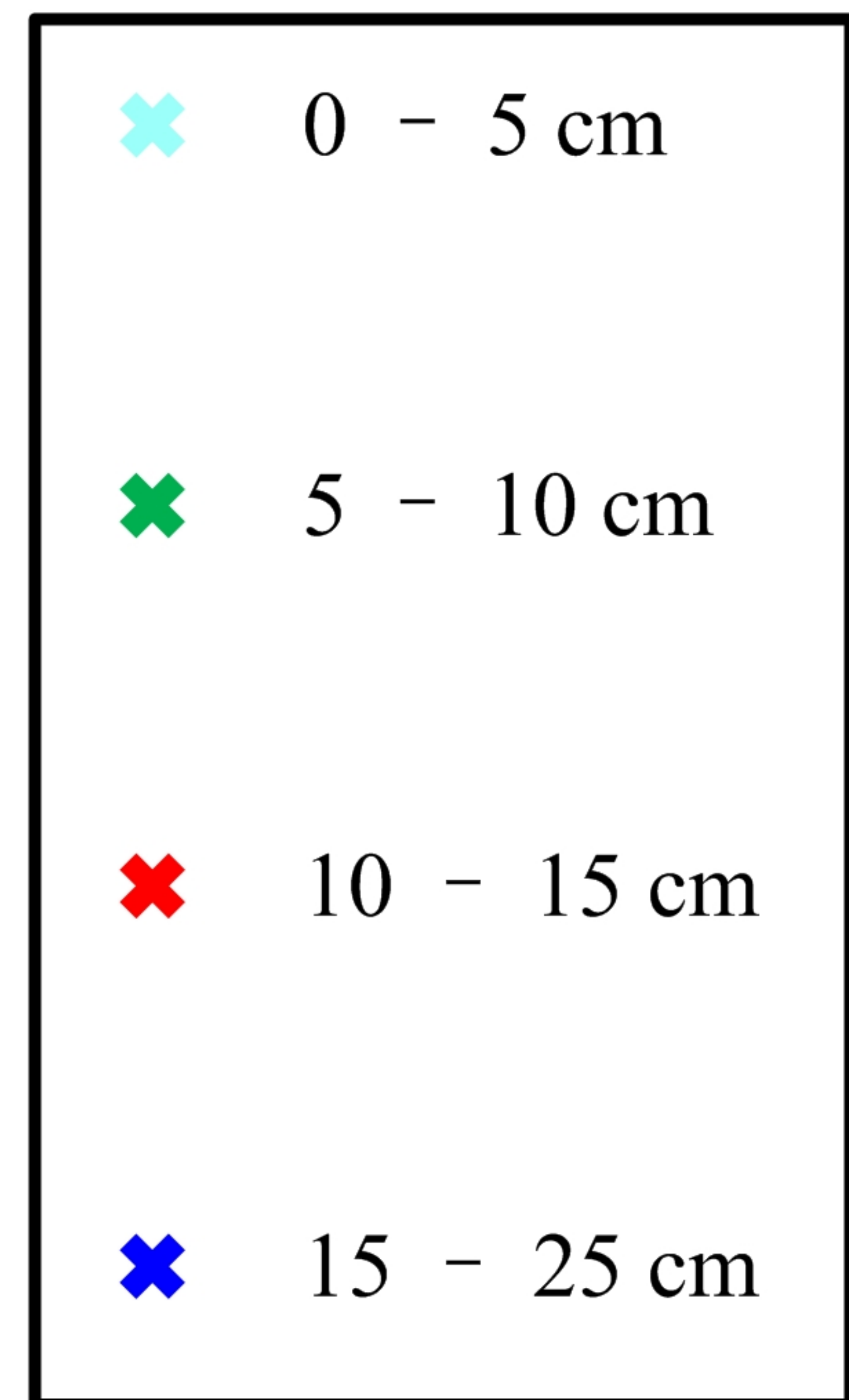
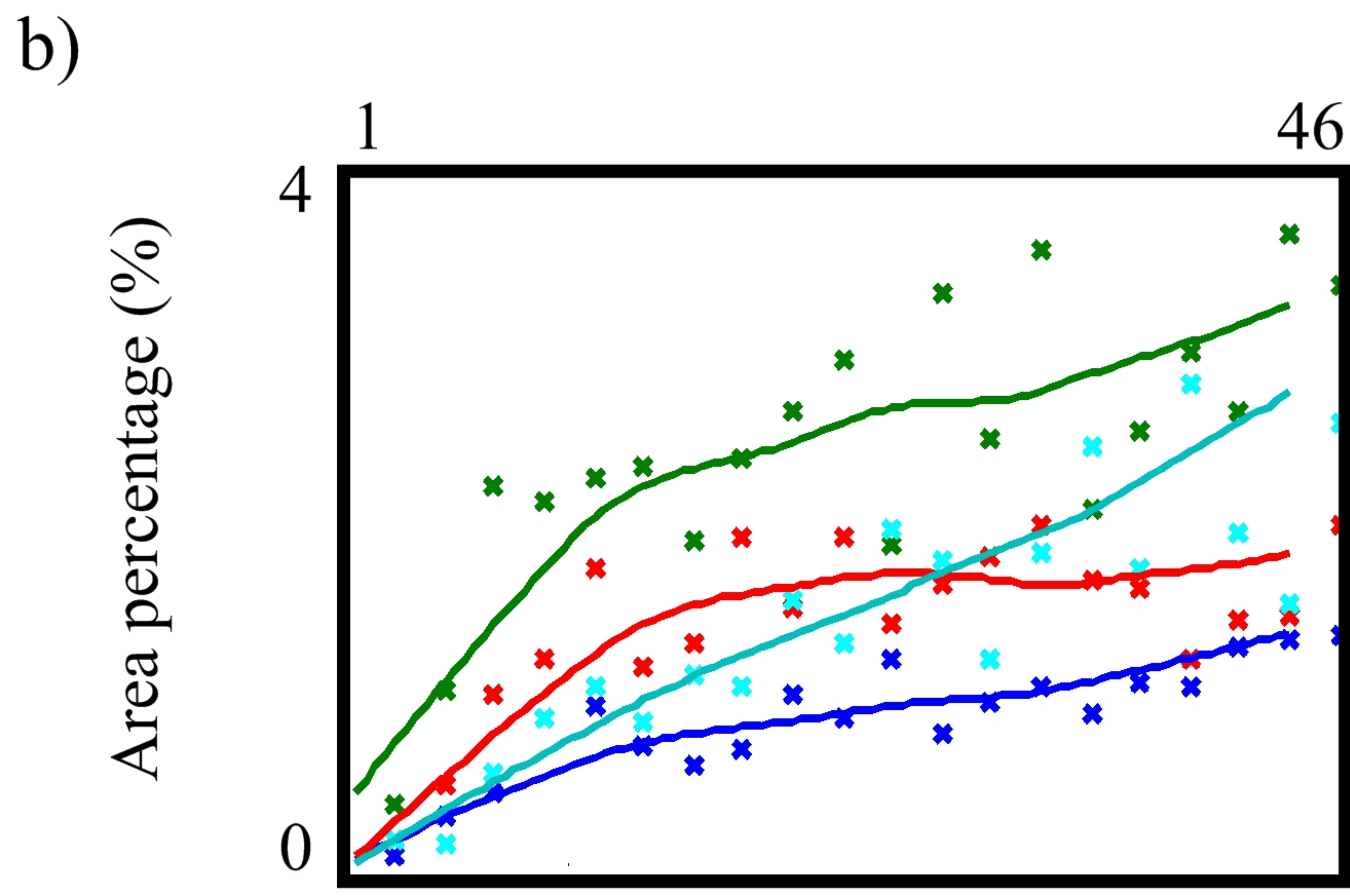
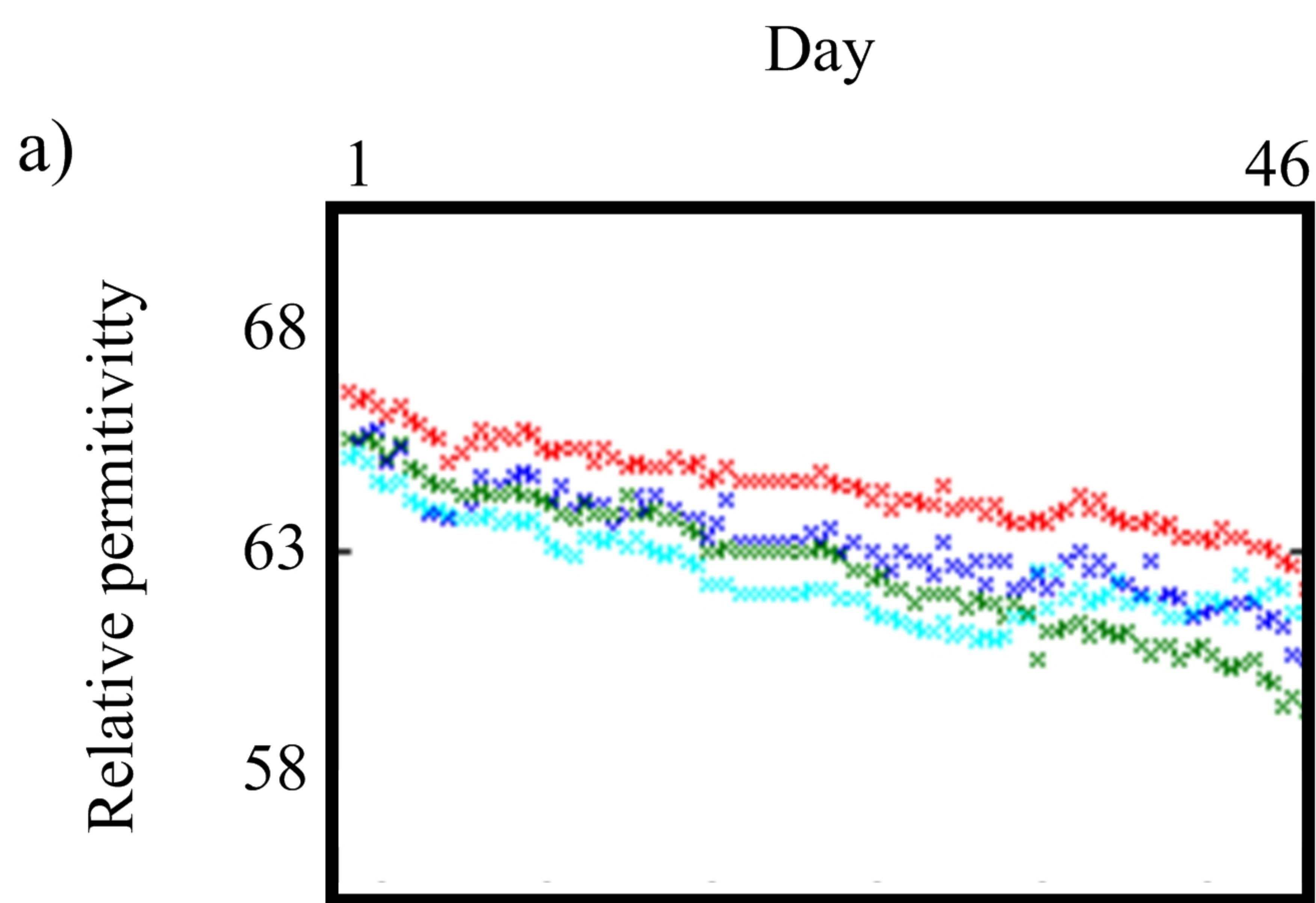
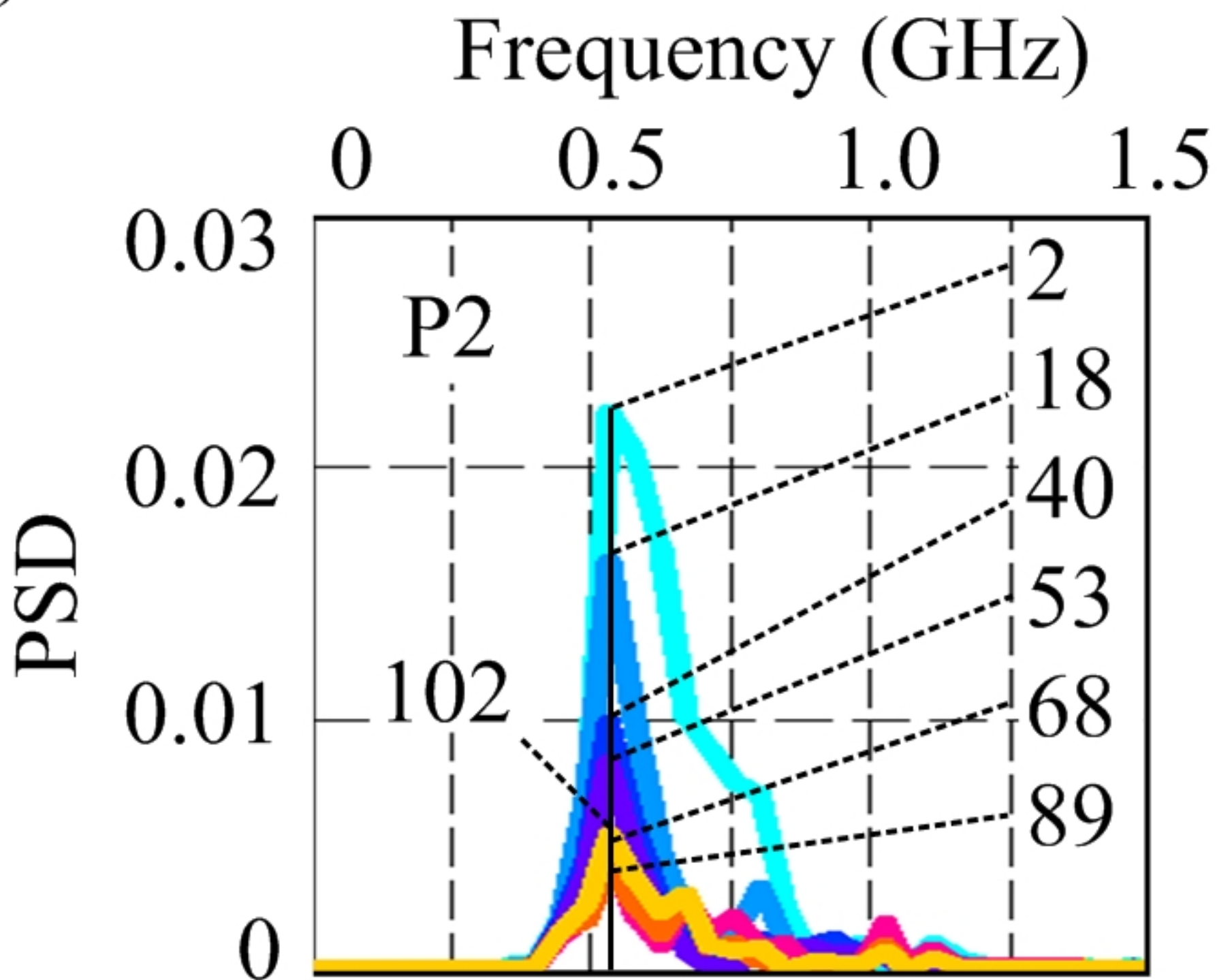


Figure 7.

a)



b)

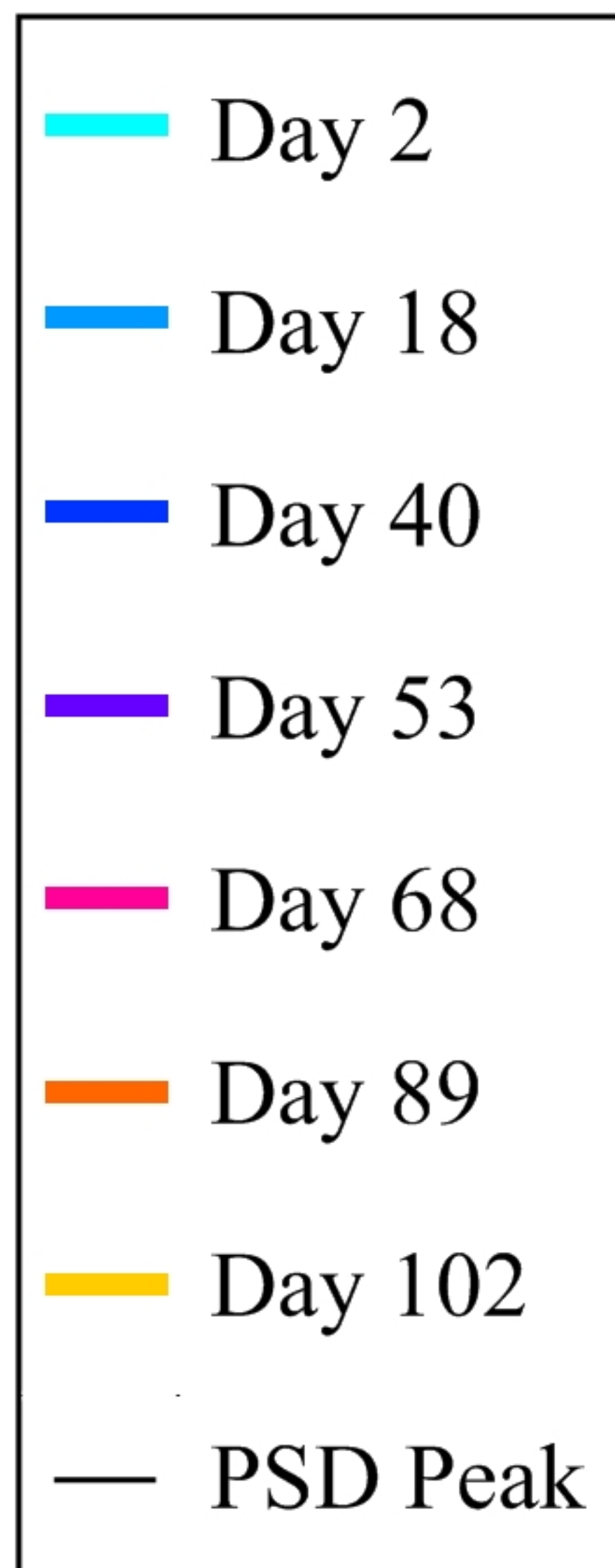
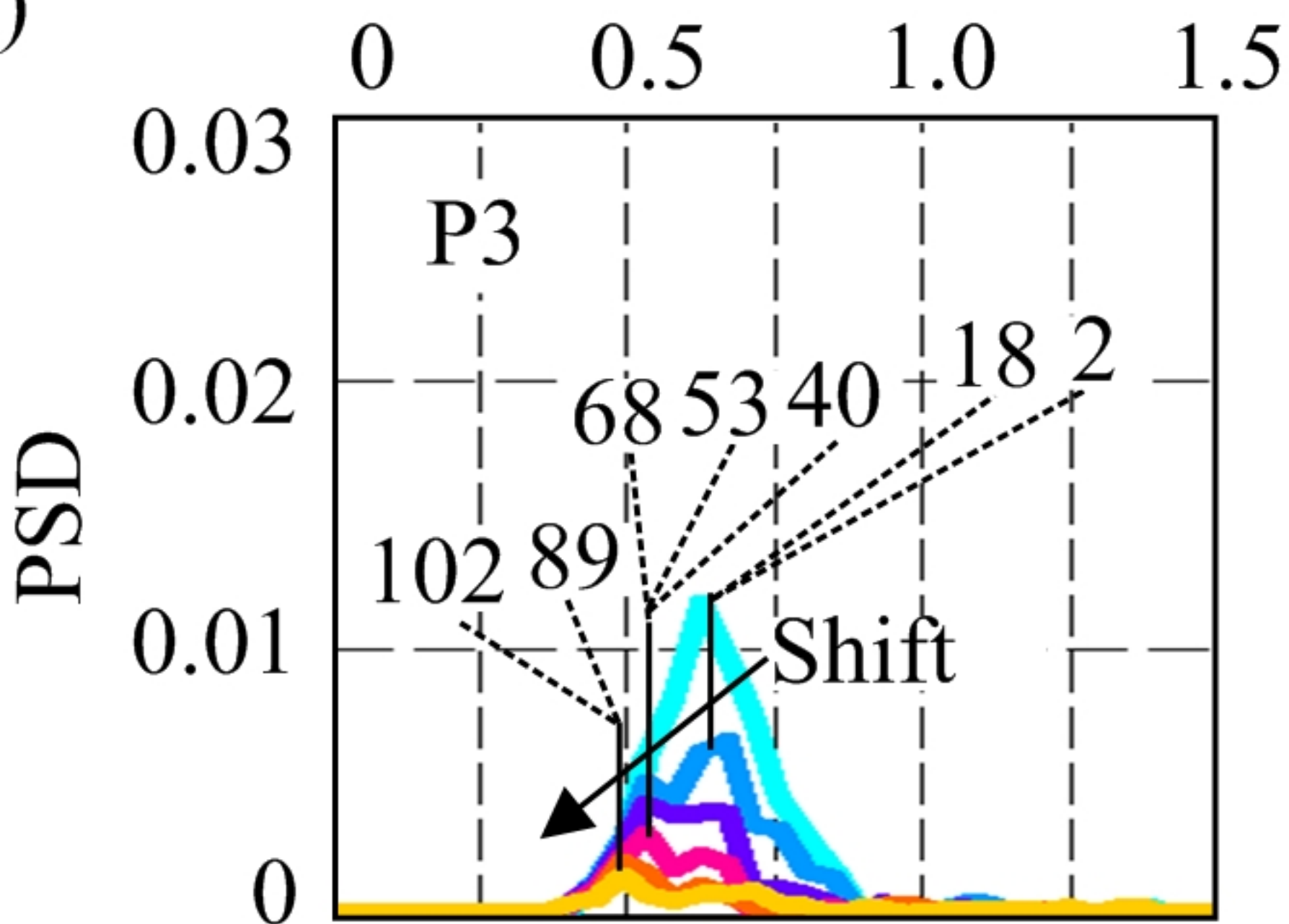


Figure 8.

